Pergamon

Int. J. Solids Structures Vol. 31, No. 12/13, pp. 1657–1693, 1994
Elsevier Science Ltd
Printed in Great Britain
0020-7683/94 $7.00 + .00

0020-7683(93)E0017-C

THERMAL ASPECTS OF MACHINING: A BEM APPROACH

ABHIJIT CHANDRA and CHO LIK CHAN
Department of Aerospace and Mechanical Engineering, The University of Arizona, Tucson, AZ 85721 U.S.A.

Abstract—Elevated temperatures generated in machining operations significantly influence the chip formation mechanics, the process efficiency and the surface quality of the machined part. A BEM approach is used here to analyse the thermal aspects of machining processes. Particular attention is given to modeling of the tool-chip, chip-workpiece, and tool-workpiece interfaces. An exact expression for matching the boundary conditions across these interfaces is developed to avoid any iterations. A direct differentiation approach (DDA) is used to determine the sensitivities of temperature and flux distributions with respect to various design parameters.

The numerical results obtained by the BEM are first verified against existing analytical and FEM results. The temperature and flux fields for various machining conditions, along with their sensitivities, are presented next. The situations of progressive flank and crater wear of the tool with continued machining are also considered, and their effects on thermal fields are investigated. The BEM is found to be very robust and efficient for this class of steady-state conduction–convection problems. The application of DDA with BEM allows efficient determination of design sensitivities and avoids strongly singular kernels. This approach also provides a new avenue toward efficient optimization of the thermal aspects of machining processes.

1. INTRODUCTION

In machining operations, the elevated temperature fields generated by the severe inelastic deformations in the shear plane, along with the frictional conditions at the chip-tool interfaces, play crucial roles in determining the chip formation mechanics. Accordingly, the elevated temperature fields have significant effects on the surface quality of the finished product and the process efficiency. Tool life, as limited by its wear, depends to a large extent on the temperature in the vicinity of the cutting edge, which in turn imposes a practical limit on the rate of material removal. Excessive temperatures may lead to various types of surface damage. The shear zone temperatures in metal cutting influence the deformation processes, the occurrence of instabilities, and the behavior of free machining inclusions (Lemaire and Backofen, 1972; Von Turkovich, 1972; Ramalingam *et al.*, 1977).

There exist various analytical (Loewen and Shaw, 1954; Bhattacharyya, 1984; Shaw, 1984) and finite element analyses (Tay *et al.*, 1974; Muraka *et al.*, 1979; Stevensen *et al.*, 1983; Dawson and Malkin, 1984) of heat conduction with moving or stationary heat sources, together with kinematic, geometric and energetic aspects of the metal cutting process. The widely used analytical model of Loewen and Shaw (1954) for orthogonal machining is based on the superposition of two planar heat sources, one at the shear plane and the other at the chip-tool interface. At each location, two temperature solutions are obtained, one for each side of the planar heat source, with a fraction of the total heat going to one side and the rest going to the other. At the shear plane, the temperature solution for the workpiece side is obtained by approximating the shear plane as a band heat source moving on the surface of a stationary semi-infinite solid at the shear velocity inclined at the shear angle to the cutting velocity. The remainder of the shearing energy not entering the workpiece is assumed to cause uniform heating of the chip. The partitioning of the total shearing energy between the workpiece and the chip may be obtained by equating the temperature along the shear plane from the workpiece side to that from the chip side. Thus, the average shear plane temperature may be determined by substituting the appropriate portion of the total shearing energy into either temperature solution. A similar procedure is also used to calculate the temperature rise at the chip-tool interface.

In the analytical models, it is often assumed that the chip is formed instantaneously at the shear plane, so that a uniform plane heat source and velocity discontinuity may be

assumed to exist there. The second deformation zone has usually been neglected, and the chip-tool frictional heat source is typically assumed to be uniform.

The finite element analyses of Tay *et al.* (1974) and Stevensen *et al.* (1983) account for the primary and secondary zones arising from the fact that plastic deformation takes place over substantial zones both around the shear plane and the rake face of the tool. Dawson and Malkin (1984) have modified the heat transfer model of Loewen and Shaw (1954) for shear plane temperatures. Instead of moving the band heat source along the shear plane (relative to the workpiece), they move it at the cutting velocity, directly into the workpiece material to be removed ahead of shear plane. Thus, preheated material directly ahead of the shear plane is removed. Accordingly, part of the heat entering the workpiece at the shear plane is subsequently removed by convection before it can be conducted downward below the path of the advancing cutting edge. Dawson and Malkin (1984) also consider the energy carried off by the chip due to heat convection from the workpiece across the shear plane. Muraka *et al.* (1979) have investigated the influence of several process variables, such as flank wear rate, coolant water, etc. on the temperature distributions in orthogonal machining using the finite element method.

The boundary element method is another powerful general purpose method (Banerjee and Butterfield, 1981; Mukherjee, 1982; Brebbia *et al.*, 1984; Beskos, 1987). It is far more tolerant of aspect ratio degradation than the FEM and can yield secondary variables as accurately as the primary ones. The temperature distributions in machining processes vary sharply in the vicinity of the cutting zones. This requires very careful refinements in the FEM mesh. In BEM, however, the internal equations are applied pointwise. Thus, sharp temperature gradients over the domain may be easily captured. In metal cutting operations, the crucial quantities are typically on the boundary, and BEM provides an accurate and efficient means for obtaining them. Recently, BEM has been applied to several steady-state and transient heat conduction problems including moving boundary phase change problems (O'Neill, 1983; Curran *et al.*, 1986; Fleuries and Predeleanu, 1987; Zabaras and Mukherjee, 1987). Tanaka *et al.* (1986) have also obtained mixed boundary element solutions of steady-state convection diffusion problems in three dimensions and found the accuracy of the BEM solutions compared to exact solutions to be almost independent of the Peclet number. The BEM solutions were also unconditionally stable in space. These features make the BEM superior to domain-type numerical techniques, which have a criterion for numerical stability and whose accuracy depends to some extent on the Peclet number. Recently, Chan and Chandra (1991a) have also performed a boundary element analysis of steady-state metal cutting operations. Special attention was paid to the interface conditions at the tool-workpiece, tool-chip, and chip-workpiece interfaces, and a complete heat transfer model of steady-state turning has been obtained by matching the boundary conditions across the interfaces.

Typically, optimal designs of metal cutting operations must be carried out by nonlinear programming methods. Such algorithms require repeated iterations on the design variables, which may contain shape parameters, process parameters and material parameters. Even for a very simple metal cutting process, such a procedure can be extremely computer intensive. A crucial ingredient for obtaining successful and economical solutions to such optimization problems is the accurate determination of design sensitivities.

A large amount of literature also exists on evaluation of design sensitivity coefficients, particularly in linear problems of solid mechanics. In an article such as this, it is very difficult to acknowledge all the worthwhile contributions in this field. Instead, the reader is referred to a comprehensive book by Haug *et al.* (1986). More recently, Tsay and Arora (1988) used FEM analysis to obtain design sensitivities in nonlinear structures with history-dependent effects, and Mukherjee and Chandra (1989, 1991) obtained BEM formulations for design sensitivities in problems involving material as well as geometric nonlinearities.

In general, two methods emerge as the most powerful ones for the determination of design sensitivities. These are the direct differentiation approach (DDA) and the adjoint structure approach (ASA). The DDA typically starts from a variational equation like the principle of virtual work (e.g. Tsay and Arora, 1988) or from boundary integral equations (Mukherjee and Chandra, 1989, 1991). Such an equation is differentiated with respect to

the design variables, and the resulting equations are solved in order to obtain the sensitivities. The ASA, on the other hand, defines adjoint structures whose solutions permit explicit evaluation of the sensitivity coefficients (e.g. Haug *et al.*, 1986).

The DDA, in conjunction with the BEM, provides an extremely elegant approach toward determination of design sensitivities. The differentiation procedure developed by Barone and Yang (1988) and by Mukherjee and Chandra (1989, 1991) does not increase the singularity of the relevant kernels. Thus, while for two-dimensional problems one usually starts with kernels that are $\ln r$ and $1/r$ singular (r being the distance between a source and a field point), the differentiated kernels are regular and $1/r$ singular, respectively.

Recently, Saigal *et al.* (1989) developed a BEM strategy for sensitivity analysis of linear elasticity problems. There, the BEM equations are discretized first. Appropriate modes are then used on the discretized version to avoid direct numerical evaluation of kernels with $1/r$ singularity. Finally, the discretized BEM equations are used again for indirect evaluation of singular kernels arising in the sensitivity equations. In the present work, the approaches of Mukherjee and Chandra (1989, 1991) and Rice and Mukherjee (1990) are followed. Appropriate modes are first used to modify the BEM equations, and the modified BEM equations of steady-state conduction–convection are then differentiated with respect to design variables. Very recently, Chandra and Chan (1992) developed a design sensitivity formulation for the conduction–convection equation using the direct differentiation approach. Numerical results are compared with analytical solutions for uniform compression problems. The numerical results obtained from the BEM agree very well with those obtained analytically. Currently, at the University of Arizona, work on extension of the BEM sensitivity formulation to machining problems is in progress. Preliminary results (Chan and Chandra, 1991c) seem very encouraging.

This chapter begins with a BEM formulation for steady-state conduction–convection problems suitable for analysing machining processes. A description of the numerical implementation for planar problems follows. Particular attention is paid to modeling of the boundary conditions at the tool-chip, chip-workpiece, and workpiece-tool interfaces. An exact expression for matching is developed to satisfy the matching interface conditions without any iterations. Numerical results for BEM analyses of the thermal aspects of machining processes are presented. The results obtained by BEM are compared to existing analytical and FEM results with regard to accuracy and efficiency.

The issues relating to design sensitivities are addressed next. A BEM formulation is developed for determining the sensitivities of the thermal fields with respect to various geometric, material and process parameters. Numerical implementations of the BEM sensitivity formulation are discussed. The BEM sensitivity algorithm is first applied to the case of uniform compression of an initially square domain, for which an analytical solution exists. The BEM results are compared to the analytical results with regard to accuracy. Various machining situations, such as nonuniform chip thickness, gradual nose wear of the tool, and gradual flank and crater wear are also considered. For these cases, the design sensitivity results obtained from BEM are compared to those obtained from finite difference schemes.

2. BOUNDARY ELEMENT FORMULATION

For metal cutting processes, various tool force measurements and cine-photographs confirm that the machining process is essentially steady for a continuous strip (Tay *et al.*, 1974; Stevenson *et al.*, 1983; Bhattacharyya, 1984; Shaw, 1984). The grain sizes of the work material and the tool material are also quite small compared to the sizes of the deformation zones. Hence, the workpiece, the tool and the chip may be treated as continua that are homogeneous and isotropic. It is also reasonable to assume that thermal conductivity, specific heat and density remain constant over the operating range of a typical metal cutting process (Tay *et al.*, 1974; Muraka *et al.*, 1979; Stevenson *et al.*, 1983; Bhattacharyya, 1984; Dawson and Malkin, 1984; Shaw, 1984). Hence, the governing equation for temperature distributions in steady-state turning operations may be expressed as:

$$\rho c \mathbf{v}_i^{(s)} \frac{\partial T}{\partial x_i} = k \frac{\partial^2 T}{\partial x^2} \quad \text{in} \quad \Omega, \tag{1}$$

where T is the temperature, k is the thermal conductivity, ρ is the density, c is the heat capacity, and $\mathbf{v}_i^{(s)}$ is the scanning velocity. Here, the convention that repeated indices represent summation over the two directions is used. The boundary conditions are

$$T = \bar{T} \quad \text{on} \quad \Gamma_T, \tag{2}$$

and

$$k \frac{\partial T}{\partial x_i} n_i = \bar{q} \quad \text{on} \quad \Gamma_q. \tag{3}$$

Equation (1) applies to a Eulerian reference frame that remains spatially fixed while material flows through it. The convective term represents the energy transported by the material as it moves through the reference frame. The surface flux $\bar{q}$ includes a contribution from convection cooling losses, $q^{(c)}$, which may be written as

$$q^{(c)} = h(T - T_\infty). \tag{4}$$

Let us also consider the adjoint equation

$$-\rho c \mathbf{v}_i^{(s)} \frac{\partial G}{\partial x_i} = k \frac{\partial^2 G}{\partial x_i^2} + \delta[x_i(q) - x_i(p)], \tag{5}$$

where p is a source point and q is the field point in the domain. P and Q represent a source point and a field point, respectively, on the boundary. Applying the divergence theorem, an integral representation of the governing equations may be obtained (Tanaka *et al.*, 1986) as

$$T(p) = -k \int_\Gamma \left(\frac{\partial G(p,Q)}{\partial n_Q} T(Q) - G(p,Q) q^{(n)}(Q) \right) \mathrm{d}\Gamma - \rho c \int_\Gamma G(p,Q) T(Q) \mathbf{v}_i^{(s)} n_i(Q) \, \mathrm{d}\Gamma + \rho c \int_\Omega G(p,Q) T(q) \mathbf{v}_{i,i}^{(s)}(q) \, \mathrm{d}\Omega \tag{6}$$

and

$$q^{(n)}(Q) = \frac{\partial T(Q)}{\partial n_Q}.$$

Here, a comma denotes field point differentiation. The domain integral in eqn (6) vanishes if the scanning velocity is constant. For metal cutting operations, the scanning velocity is equal to the cutting speed, which is typically constant for a particular operation. Hence, the domain integral in eqn (6) need not be considered for present purposes. In turning operations, the scanning velocities for the tool, the workpiece, and the chip are different from each other. This, however, may be easily handled by considering three separate regions. As discussed in a later section, the complete temperature distribution in the tool, the workpiece, and the chip may then be obtained by appropriate matching.

The fundamental solution $G(p,q)$ (Carslaw and Jaeger, 1986; Tanaka *et al.*, 1986) is given as

$$G(p,q) = \frac{1}{2\pi k} \exp\left\{\frac{\mathbf{v}_i^{(s)}[x_i(q) - x_i(p)]}{2\kappa}\right\} K_0\left(\frac{vr}{2\kappa}\right) \text{ in two dimensions.} \tag{7}$$

Here, v is the magnitude of the scanning velocity vector $\mathbf{v}_i^{(s)}$, r is the distance between the source point and the field point, and K_0 is the modified Bessel function of the second kind of order zero.

A boundary integral equation for the steady-state conduction–convection problem may now be obtained by taking the limit as p tends to P. This gives

$$C(P)T(P) = -k\int_\Gamma \left[\frac{\partial G(P,Q)}{\partial n_Q} T(Q) - G(P,Q)q^{(n)}(Q)\right] d\Gamma - \rho c \int_\Gamma G(P,Q)T(Q)\mathbf{v}_i^{(s)} n_i(Q)\, d\Gamma. \tag{8}$$

The coefficient C, in general, depends on the local geometry at P. If the boundary is locally smooth at P, $C = 1/2$. Otherwise, it may be evaluated indirectly (Banerjee and Butterfield, 1981; Mukherjee, 1982; Brebbia *et al.*, 1984).

2.1. *Numerical implementation*

Numerical implementation of the BEM eqns (6)–(8) for the conduction–convection problem is discussed in this section. The first step is the discretization of the boundary of the two-dimensional domain into boundary elements. A discretized version of the boundary integral eqn (8) may be written as (Banerjee and Butterfield, 1981; Mukherjee, 1982; Brebbia *et al.*, 1984)

$$C(P_M)T(P_M) = -k\sum_{i=1}^{N_s} \int_{\Delta s_i} \left[\frac{\partial G(P_M,Q)}{\partial n_Q} T(Q) - G(P_M,Q)q^{(n)}(Q)\right] ds_Q - \rho c \sum_{i=1}^{N_s} \int_{\Delta s_i} G(P_M,Q)T(Q)v_i^{(s)} n_i(Q)\, ds_Q, \tag{9}$$

where the boundary of the domain Γ is divided into N_s boundary segments and $T(P_M)$ represents temperature at a point P that coincides with mode M.

A suitable shape function must now be chosen for the variation of temperature and flux over the boundary elements Δs_i. In the present work, both temperature and flux are assumed to be linear over individual boundary elements. Hence, eqn (9) may be written as:

$$C(P_M)T(P_M) = -\sum_{i=1}^{N_s} \int_{\Delta s_i} \left[k\frac{\partial G(P_M,Q)}{\partial n_Q} + \rho c G(P_M,Q)v_i^{(s)} \cdot n_i(Q)\right] + k\sum_{i=1}^{N_s} \int_{\Delta\sigma_i} G(P_M,Q)(\psi_1 q_1^{(n)} + \psi_2 q_2^{(n)})\, ds_Q, \tag{10}$$

where the shape functions

$$\psi_1 = \tfrac{1}{2}(1-\eta) \quad \text{and} \quad \psi_2 = \tfrac{1}{2}(1+\eta) \tag{11}$$

and η is the dimensionless local coordinate over individual boundary segments. T_1, T_2, $q_1^{(n)}$, and $q_2^{(n)}$ are the nodal quantities of the ith boundary segment.

Defining

$$a^{\gamma}_{Mj} = c_M \delta_{Mj} + \int_{\Delta s_j} \psi_\gamma \left[k \frac{\partial G(P_M, Q)}{\partial n_Q} + \rho c G(P_M, Q) v_\ell^{(s)} n_\ell \right] \mathrm{d}s_Q \tag{12}$$

and

$$b^{\gamma}_{Mj} = -k \int_{\Delta s_j} \psi_\gamma G(P_M, Q)\, \mathrm{d}s_Q. \tag{13}$$

Equation (10) may now be expressed as

$$\sum_{j=1}^{N_s} A_{ij} T_j + \sum_{j=1}^{N_s} B_{ij} q_j^{(n)} = 0, \tag{14}$$

where N_s is the total number of boundary nodes and each nodal coefficient A_{ij} is equal to the sum of a_{ij}^2 of element $(j-1)$ and a_{ij}^1 of element (j) for an anticlockwise numbering system. The same procedure also applies to B_{ij}.

Integrals of kernels over elements in eqns (12)–(13) must be obtained carefully. In the present work, the diagonal elements of $G(P_M, Q)$ which are log (r) singular may be evaluated numerically through an algorithm for improper integrals (Press *et al.*, 1986). The proper combination of the constant $C(P_M)$ and the diagonal elements of $\partial G(P_M, Q)/\partial n_Q$ is evaluated indirectly by applying isothermal boundary conditions over the entire boundary (Banerjee and Butterfield, 1981; Mukherjee, 1982; Brebbia *et al.*, 1984).

At each location over the entire boundary of the domain, either T, $q^{(n)}$, or a combination of T and $q^{(n)}$ [see eqns (2)–(4)] is prescribed for a well-posed problem. Equation (14) may be rearranged as

$$\sum_{j=1}^{N_s} \tilde{A}_{ij} \mathbf{Y}_j^{(u)} + \sum_{j=1}^{N_s} \tilde{B}_{ij} \mathbf{Y}_j^{(k)} = 0. \tag{15}$$

The matrix coefficients $\tilde{A}_{ij}$ and $\tilde{B}_{ij}$ in eqn (15) are

$$\tilde{A}_{ij} = \begin{cases} A_{ij}, & \text{for } q_j^{(n)} \text{ specified} \\ B_{ij}, & \text{for } T_j \text{ specified} \\ A_{ij} + B_{ij} h, & \text{for convective heat loss} \end{cases}, \tag{16}$$

$$\tilde{B}_{ij} = \begin{cases} B_{ij}, & \text{for } q_j^{(n)} \text{ specified} \\ A_{ij}, & \text{for } T_j \text{ specified} \\ -B_{ij} h, & \text{for convective heat loss} \end{cases}, \tag{17}$$

and the column vectors $\mathbf{Y}_j^{(u)}$ and $\mathbf{Y}_j^{(k)}$ are

$$\mathbf{Y}_j^{(u)} = \begin{bmatrix} T_j, & \text{for } q_j^{(n)} \text{ specified, or for convective heat loss} \\ q_j^{(n)}, & \text{for } T_j \text{ specified} \end{bmatrix}, \tag{18}$$

$$\mathbf{Y}_j^{(k)} = \begin{cases} q_j^{(n)}, & \text{for } q_j^{(n)} \text{ specified} \\ T_j, & \text{for } T_j \text{ specified} \\ T_\infty, & \text{for convective heat loss} \end{cases}. \tag{19}$$

Equation (15) can now be used to solve for the unknown temperature and flux. Once T and $q^{(n)}$ have been obtained over the entire boundary, the internal eqn (6) may be used to obtain temperature and flux at any internal point.

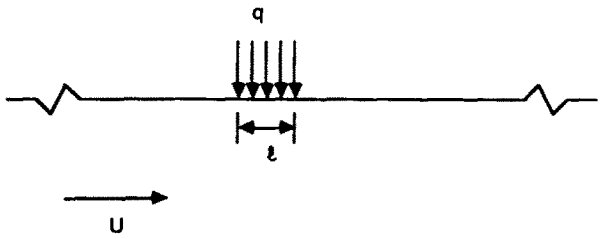

Fig. 1. Schematic diagram of the Jaeger solution.

2.2. *Verification of the conduction–convection algorithm*

The BEM formulation is first applied to calculate the surface temperature of a semi-infinite domain with surface heating over a finite region. This corresponds to the well-known Jaeger solution (Jaeger, 1942). A schematic design of the Jaeger problem is given in Fig. 1. Introducing the dimensionless variables,

$$\tilde{x}_i = \frac{x_i}{\ell} \quad \text{and} \quad \tilde{T} = \frac{T - T_\infty}{q\ell/k}, \tag{20}$$

the governing equation in dimensionless form is

$$\frac{\partial \tilde{T}}{\partial \tilde{x}_1} = \frac{1}{Pe}\left(\frac{\partial^2 \tilde{T}}{\partial \tilde{x}_1^2} + \frac{\partial^2 \tilde{T}}{\partial \tilde{x}_2^2}\right), \tag{21}$$

$$\tilde{x}_2 = 0, \quad \frac{\partial \tilde{T}}{\partial \tilde{x}_2} = \begin{cases} -1 & 0 \leqslant \tilde{x}_1 \leqslant 1 \\ 0 & \text{otherwise} \end{cases}, \tag{22}$$

$$|\tilde{x}_1|, \quad \tilde{x}_2 \to \infty, \quad \tilde{T} = 0, \tag{23}$$

where

$$Pe = \frac{U\ell}{\kappa}. \tag{24}$$

The surface temperatures underneath the surface heat flux for four different Peclet numbers are plotted in Fig. 2. It can be observed that the BEM solutions compare very

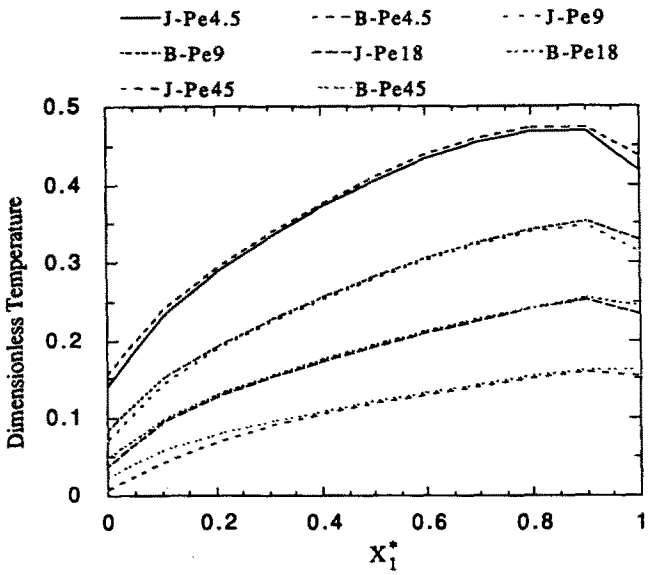

Fig. 2. The Jaeger solution—comparison between the BEM and the analytical method (J = Jaeger; B = BEM).

well to the corresponding Jaeger solutions, with a maximum discrepancy of 10% over a range of Peclet numbers from 4.5 to 45. We have also compared the BEM solutions to other analytical solutions, such as the thermal entrance length of the slug flow problem. The BEM solutions co-related well with the analytical solutions.

3. MODELING OF MACHINING PROCESSES

In this section, the BEM formulation is used to model a steady-state metal cutting process. Typically, the tool is a large-angled wedge that is driven into the workpiece to remove a thin layer, the chip. A schematic diagram of the process is sketched in Fig. 3. As the tool is driven into the workpiece, the material undergoes a severe plastic deformation along the shear plane. As the chip forms, it diverts and slides across the tool face. There are two main sources of heat generation: (1) the heat generated by the plastic deformation in the shear plane—the primary zone—and (2) the frictional heating and plastic deformation as the chip slides over the tool face—the secondary zone. The heat transfer involved here is conduction and convection of the heat generated into the tool, the chip, and the workpiece.

In a metal cutting operation, the velocities associated with the tool, the workpiece and the chip are quite different. Fixing the reference frame to the tool, it may be considered stationary. The workpiece, with respect to such a reference frame, moves at the cutting velocity (scanning velocity). The chip moves in a different direction with a velocity related to the scanning and the shear plane angle. Consequently, the BEM algorithm is applied to each region separately. For oblique cutting, the chip velocity may also depend on the tool angles. Consequently, the previously developed BEM algorithm is applied separately to each of the regions. By matching the boundary conditions at the workpiece-chip interface and the chip-tool interface, a complete solution for the metal cutting problem may then be obtained.

3.1. *Mathematical formulation*

Here, orthogonal machining is considered and a two-dimensional analysis of heat transfer is performed. In order to model the heat transfer efficiently, the tool, the chip and the workpiece are formulated separately. Furthermore, a coordinate system unique to each region is defined for the purpose of better boundary element representation. The coordinate systems for the three regions are defined in Fig. 4. The mathematical formulation for the conduction–convection heat transfer within each region is now presented in their dimensionless form. The relevant scales are ℓ as the length scale, $q'\ell/k_w$ as the temperature scale, and q' as the heat flux scale.

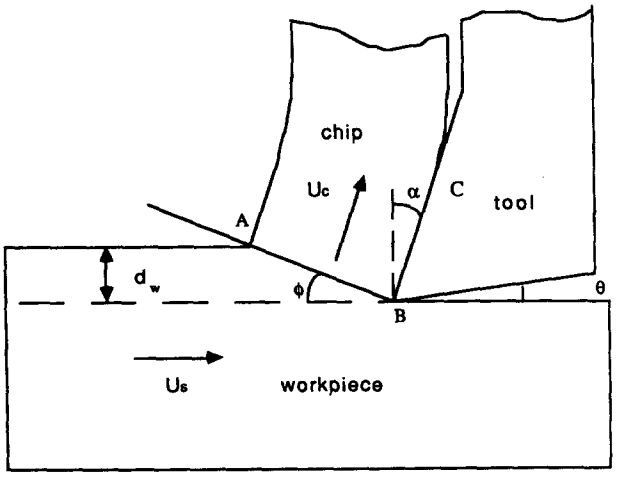

Fig. 3. Schematic diagram of metal cutting process.

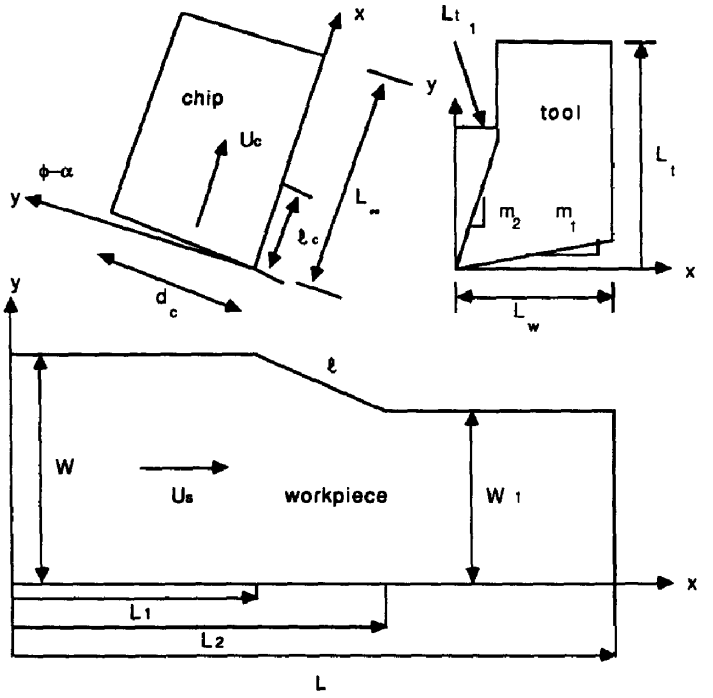

Fig. 4. Coordinate system for each region.

3.1.1. *Within the workpiece.*

$$\frac{\partial \tilde{T}_w}{\partial \tilde{X}} = \frac{1}{Pe_w}\left(\frac{\partial^2 \tilde{T}_w}{\partial \tilde{X}^2} + \frac{\partial^2 \tilde{T}_w}{\partial \tilde{Y}^2}\right) \quad \text{in} \quad \tilde{\Omega}_w, \tag{25}$$

$$Pe_w = \frac{v_s \ell}{\kappa_w}. \tag{26}$$

The coordinate system is chosen so the scanning velocity aligns with the x_w-direction. The boundary conditions appropriate for the present region are

$$\tilde{X} = 0; \quad \tilde{T}_w = 0, \tag{27}$$

$$\tilde{X} = \tilde{L}; \quad \frac{\partial \tilde{T}_w}{\partial \tilde{X}} = 0, \tag{28}$$

$$\tilde{Y} = 0; \quad \tilde{T}_w = 0, \tag{29}$$

$$\tilde{Y} = \tilde{W}, 0 \leqslant \tilde{X} \leqslant \tilde{L}_1; \quad \frac{\partial \tilde{T}_w}{\partial \tilde{Y}} = -Nu_w \tilde{T}, \tag{30}$$

$$\tilde{Y} = \tilde{W}_1, \tilde{L}_2 \leqslant \tilde{X} \leqslant \tilde{L}; \quad \frac{\partial \tilde{T}_w}{\partial \tilde{Y}} = -Nu_w \tilde{T}_w, \tag{31}$$

$$Nu_w = \frac{h_w \ell}{k_w}. \tag{32}$$

The first boundary condition, eqn (27), means that the incoming materials are at the ambient temperature. Equation (28) implies that beyond a certain distance downstream the

heat transfer in the x_w-direction is negligible. Equation (29) means that far away from the source the material is not affected. Equations (30) and (31) represent the convective heat loss to the ambient. The boundary condition along the shear plane has to match with that of the chip and will be discussed at a later time.

3.1.2. *Within the chip.* The governing equation within the chip is

$$\frac{\partial \tilde{T}_c}{\partial \tilde{x}_c} = \frac{1}{Pe_c}\left(\frac{\partial^2 \tilde{T}_c}{\partial \tilde{x}_c^2} + \frac{\partial^2 \tilde{T}_c}{\partial \tilde{y}_c^2}\right) \quad \text{in} \quad \tilde{\Omega}_c, \tag{33}$$

$$Pe_c = \frac{v_c \ell}{\kappa_c} = Pe_w \frac{\mathrm{d}_w \kappa_w}{\mathrm{d}_c \kappa_c}. \tag{34}$$

Once again, the coordinate system is chosen so the motion of the chip is aligned with the x_c-direction. It should be pointed out that the chip usually curls up. However, if the thickness of the chip is much smaller than the radius of curvature of the curling, the Cartesian coordinate form of equations can be used to approximate the problem. The boundary conditions appropriate in this region are

$$\tilde{x}_c = \tilde{L}_\infty; \quad \frac{\partial \tilde{T}_c}{\partial \tilde{x}_c} = 0, \tag{35}$$

$$\tilde{y}_c = 0, \tilde{\ell}_c \leqslant \tilde{x}_c \leqslant \tilde{L}_\infty; \quad \frac{\partial \tilde{T}_c}{\partial \tilde{y}_c^2} = Nu_c \tilde{T}_c, \tag{36}$$

$$\tilde{y}_c = \tilde{\mathrm{d}}_c, \tilde{\mathrm{d}}_c \tan(\phi - \alpha) \leqslant \tilde{x}_c \leqslant \tilde{L}_\infty; \quad -\frac{\partial \tilde{T}_c}{\partial \tilde{y}_c^2} = Nu_c \tilde{T}, \tag{37}$$

$$Nu_c = \frac{h_c \ell}{k_c}. \tag{38}$$

The first boundary condition, eqn (35), means that at a certain distance from the shear plane the heat loss through the chip is negligible. Equations (36)–(37) represent convective heat loss to the ambient. The boundary condition at $x_c = 0$ is a matching condition along the shear plane, and that at $y_c = 0$ and $0 < x_c < \ell_c$ is a matching condition along the chip-tool interface; they will be discussed at a later time.

3.1.3. *Within the tool.* With respect to the reference frame chosen, the tool is stationary. Consequently, the heat transfer within this region is pure conduction. The governing equation is

$$\frac{\partial^2 \tilde{T}_t}{\partial \tilde{x}_t^2} + \frac{\partial^2 \tilde{T}_t}{\partial \tilde{y}_t^2} = 0 \quad \text{in} \quad \tilde{\Omega}_t. \tag{39}$$

The boundary conditions appropriate in this region are

$$\tilde{y}_t = m_1 \tilde{x}_t, \quad 0 \leqslant \tilde{x}_t \leqslant \tilde{L}_w; \quad \frac{\partial \tilde{T}_t}{\partial \tilde{n}_t} = -Nu_t \tilde{T}_t, \tag{40}$$

$$\tilde{x}_t = \tilde{L}_w, \quad m_1 \tilde{L}_w \leqslant \tilde{y}_t \leqslant \tilde{L}_t; \quad \frac{\partial \tilde{T}_t}{\partial \tilde{x}_t} = -Nu_t \tilde{T}_t, \tag{41}$$

$$\tilde{y}_t = \tilde{L}_t; \quad \frac{\partial \tilde{T}_t}{\partial \tilde{y}_t} = -Nu_p \tilde{T}_t, \tag{42}$$

$$\tilde{x}_t = \tilde{L}_{t_1}, \quad m_2\tilde{L}_{t_1} \leqslant \tilde{y}_t \leqslant \tilde{L}_t; \quad \frac{\partial \tilde{T}_t}{\partial \tilde{x}_t} = Nu_t\tilde{T}_t, \tag{43}$$

$$\tilde{y}_t = m_2\tilde{x}_t, \quad \tilde{L}_{t_1}/2 \leqslant \tilde{x}_t \leqslant \tilde{L}_{t_1}; \quad \frac{\partial \tilde{T}_t}{\partial \tilde{n}_t} = -Nu_t\tilde{T}_t \tag{44}$$

$$Nu_t = \frac{h_t\ell}{k_t}, \quad Nu_p = \frac{h_p\ell}{k_t}. \tag{45}$$

The first and second boundary conditions (40), (41) represent the convective heat loss to the ambient. Equation (42) represents a convective heat loss model for the heat flux going into the tool holder. Equations (43) and (44) represent the convective heat loss to the ambient. The contact length between the tool and the chip depends strongly on the cutting condition and the material properties of the tool and the workpiece. It has also been observed by Trent (1984, Chapter 9) that alloying elements have a significant influence on the chip-tool contact area. It has been observed over a wide range of experiments (Levy *et al.*, 1976; Trent, 1984) that the contact length is of the order of the length of the shear plane. In our analysis, the contact length is assumed to be 0.75 times the length of the shear plane. It should be noted, however, that the proposed scheme of analysis can handle any specified contact length that is not dependent on any particular assumption.

3.1.4. *Matching boundary conditions.* The matching boundary conditions along the shear plane and the chip-tool interface is now presented. Along the shear plane, often referred to as the primary deformation zone, heat is generated as a result of the large plastic deformation. Assuming that the rate of work in the deformation zone is converted entirely into heat, the heat generation can be calculated by the following equation (Tay *et al.*, 1974; Stevenson *et al.*, 1983; Dawson and Malkan, 1984):

$$q'\tilde{\delta}_{sp} = \tilde{\tau}\cdot\tilde{\dot{\gamma}}, \tag{46}$$

where q' is the volumetric heat generation and $\tilde{\tau}$ is the yield stress; $\tilde{\dot{\gamma}}$ is the shear strain rate, which can be calculated from

$$\tilde{\dot{\gamma}} = \frac{C_s\tilde{V}_{\text{slide}}}{\tilde{d}_w} = \frac{C_s}{\tilde{d}_w}\frac{\cos\alpha}{\cos(\phi-\alpha)}, \tag{47}$$

where C_s is an empirical constant; V_{slide} is the sliding velocity, which is related to the scanning velocity v_s, the rake angle α, and the shear plane angle ϕ; δ_{sp} is a Dirac delta function situated along the shear plane. Consequently, the heat generated is assumed to be concentrated along the shear plane. Applying an energy balance along the shear plane, the matching boundary condition can be obtained:

$$\tilde{q}^{(n)}_{\text{workpiece}} + \tilde{q}^{(n)}_{\text{chip}} = 1. \tag{48}$$

Furthermore, the continuity of temperature is also prescribed:

$$\tilde{T}_w = \tilde{T}_c. \tag{49}$$

The secondary deformation zone is located along the chip-tool interface. Heat is generated by plastic deformation and frictional heating. The actual heat generation in the secondary zone depends on the exact cutting conditions. Based on the observations of Trent (1984, Chapters 6 and 9) and Tay *et al.* (1974), for non-abrasive continuous chips and medium cutting speeds, the total heat generation due to frictional heating and plastic deformation in the secondary zone may be reasonably assumed to be between 0.20 and 0.35 times that in the primary zone. In our analysis, we have assumed the total heat generation

in the secondary zone to be 0.25 times that in the primary zone. The actual distribution needs to be determined experimentally, and the proposed analysis scheme is capable of handling any specified spatial heat generation profile. Here, both effects are modeled by a total volumetric heat generation, $q'_s\delta_{ct}$, concentrated along the chip-tool interface. Once again, applying the energy balance, the matching condition along the chip-tool interface is

$$\tilde{q}^{(n)}_{\text{chip}} + \tilde{q}^{(n)}_{\text{tool}} = q'_s/q', \tag{50}$$

and

$$\tilde{T}_c = \tilde{T}_t. \tag{51}$$

Equations (25)–(51) form the mathematical model of the heat transfer within the tool, the chip, and the workpiece during metal cutting.

3.2. *Matching scheme*

As mentioned before, the BEM algorithm is first applied to solve the heat transfer in each region separately. By matching the boundary conditions along the shear plane and the chip-tool interface, a complete solution may then be obtained. An exact expression can be derived to satisfy the matching conditions based on a guess solution. This matching scheme will now be presented.

Applying the algorithm developed in Section 2, three matrix equations of the form of eqn (15)–(19) can be derived. This equation can be interpreted as a relation between all the unknown $Y^{(n)}_j$ and the specified conditions. It is interesting, however, to note that the matrix coefficients depend only on the geometry, the fundamental solution, and the shape functions. They do not depend on either the temperature or the heat flux. Along the matching interfaces, typically, temperatures will be prescribed and fluxes will need to be evaluated. The change in the flux at the jth node due to a change in the temperature at the ℓth node can be obtained by taking the derivative of eqn (15) with respect to T_ℓ:

$$\sum_{j=1}^{N_s} \tilde{B}_{ij} \frac{\partial q^{(n)}_j}{\partial T_\ell} = -\tilde{A}_{i\ell}. \tag{52}$$

Furthermore, all the derivatives are independent of temperature and flux. Consequently, an exact linear equation can be derived as

$$q^{(n)}_j - q^{(n)(0)}_j = \sum_{\ell=\ell_1}^{\ell_2} (T_\ell - T^{(0)}_\ell) \frac{\partial q^{(n)}_j}{\partial T_\ell}. \tag{53}$$

Here, $q^{(n)(0)}_j$ is the solution of eqn (17) based on an arbitrary prescribed $T^{(0)}_\ell$. It should be noted that, depending on the desired heat flux condition, the correct temperature T_ℓ can be determined exactly from eqn (53) without recourse to any iterative scheme. Here, (ℓ_1, ℓ_2) denotes the range of the boundary nodes over which matching is required. A similar strategy has also been used by Zabaras *et al.* (1988) for inverse heat conduction problems with phase changes.

We will illustrate the matching scheme by considering two regions—the workpiece and the chip. A schematic diagram of the shear plane defining the numbering of the matching nodes is depicted in Fig. 5. Two equations similar to eqn (53) for the workpiece and the chip can be derived:

$$\tilde{q}^{(n)}_{w_j} - \tilde{q}^{(n)(0)}_{w_j} = \sum_{\ell=\ell_1}^{\ell_2} (\tilde{T}_{w_\ell} - \tilde{T}^{(0)}_{w_\ell}) \frac{\partial \tilde{q}^{(n)}_{w_j}}{\partial \tilde{T}_{w_\ell}} \quad j = \ell_1, \ldots, \ell_2, \tag{54}$$

and

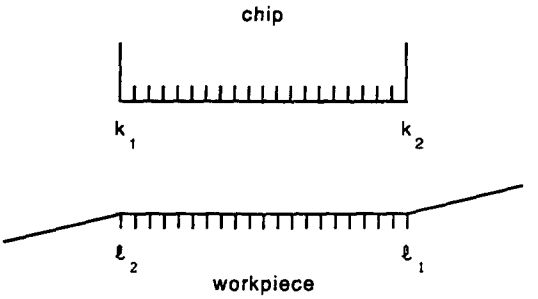

Fig. 5. Schematic diagram of matching conditions for two regions.

$$\tilde{q}^{(n)}_{c_j} - \tilde{q}^{(n)(0)}_{c_j} = \sum_{\ell=k_1}^{k_2} (\tilde{T}_{c_\ell} - \tilde{T}^{(0)}_{c_\ell}) \frac{\partial \tilde{q}^{(n)}_{c_j}}{\partial \tilde{T}_{c_\ell}}; \quad j = k_1, \ldots, k_2. \tag{55}$$

Without loss of generality, it may be assumed that the starting temperatures are

$$\tilde{T}^{(0)}_{c_{j-1+k_1}} = \tilde{T}^{(0)}_{w_{\ell_2-j+1}} = 1 \quad j = 1, \ldots, (k_2 - k_1 + 1). \tag{56}$$

The matching conditions, (48), (49), can be written as

$$\tilde{q}^{(n)}_{c_{j-1+k_1}} + \tilde{q}^{(n)}_{w_{\ell_2-j+1}} = 1 \quad j = 1, \ldots, (k_2 - k_1 + 1), \tag{57}$$

and

$$\tilde{T}_{c_{j-1+k_1}} = \tilde{T}_{w_{\ell_2-j+1}} \quad j = 1, \ldots, (k_2 - k_1 + 1). \tag{58}$$

Adding eqns (54) and (55) via (56) and substituting for the matching condition eqns (57) and (58), we have

$$1 - \tilde{q}^{(n)(0)}_{c_{j-1+k_1}} - \tilde{q}^{(n)(0)}_{w_{\ell_2-j+1}} = \sum_{\ell=1}^{k_2-k_1+1} \left(\frac{\partial \tilde{q}^{(n)}_{c_{j-1+k_1}}}{\partial \tilde{T}_{c_{\ell-1+k_1}}} + \frac{\partial \tilde{q}^{(n)}_{w_{\ell_2-j+1}}}{\partial \tilde{T}_{w_{\ell_2-\ell+1}}} \right) (\tilde{T}_{c_{\ell-1+k_1}} - \tilde{T}^{(0)}_{c_{\ell-1+k_1}}). \tag{59}$$

Equation (59) can be used to calculate the exact temperature at the appropriate interfaces.

The matching procedure for three regions will now be presented. The derivation is very similar. A schematic diagram defining the number system of the three regions is presented in Fig. 6. Equation (54) for the workpiece is still applicable. Equation (55) needs to be modified to include the additional chip-tool interface:

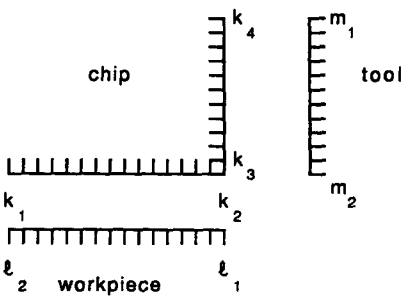

Fig. 6. Schematic diagram of matching conditions for three regions.

$$\tilde{q}_{c_j}^{(n)} - \tilde{q}_{c_j}^{(n)(0)} = \sum_{\ell=k_1}^{k_2} (\tilde{T}_{c_\ell} - \tilde{T}_{c_\ell}^{(0)}) \frac{\partial \tilde{q}_{c_j}^{(n)}}{\partial \tilde{T}_{c_\ell}} + \sum_{\ell=k_3}^{k_4} (\tilde{T}_{c_\ell} - \tilde{T}_{c_\ell}^{(0)}) \frac{\partial \tilde{q}_{c_j}^{(n)}}{\partial \tilde{T}_{c_\ell}} \quad j = k_1, \ldots, k_2 \text{ and } k_3, \ldots, k_4. \tag{60}$$

Here, $(k_1, \ldots, k_2)$ denotes the shear plane and $(k_3, \ldots, k_4)$ denotes the chip-tool interface. The first summation represents the contribution from the temperature change along the shear plane, while the second summation represents the contribution from the temperature change along the chip-tool interface. Similarly, the equation applicable for the tool region is

$$\tilde{q}_{t_j}^{(n)} - \tilde{q}_{t_j}^{(n)(0)} = \sum_{\ell=m_1}^{m_2} (\tilde{T}_{t_\ell} - \tilde{T}_{t_\ell}^{(0)}) \frac{\partial \tilde{q}_{t_j}^{(n)}}{\partial \tilde{T}_{t_\ell}}; \quad j = m_1, \ldots, m_2. \tag{61}$$

Here, $(m_1, \ldots, m_2)$ denotes the nodes located along the chip-tool interface.

The matching boundary conditions along the shear plane are given by eqns (57) and (58). The matching boundary conditions along the chip-tool interface are

$$\tilde{q}_{c_{j-1+k_3}}^{(n)} + \tilde{q}_{t_{m_2-j+1}}^{(n)} = q_s'/q' \quad j = 1, \ldots, (k_4 - k_3 + 1), \tag{62}$$

$$\tilde{T}_{c_{j-1+k_3}} = \tilde{T}_{t_{m_2-j+1}} \quad j = 1, \ldots, (k_4 - k_3 + 1). \tag{63}$$

Using the matching condition eqns (57), (58), (59), and (60), eqns (54), (60), and (61) can be combined:

for $j = k_1, \ldots, k_2$,

$$1 - \tilde{q}_{c_j}^{(n)(0)} - \tilde{q}_{w_{\ell_2-j+k_1}}^{(n)(0)} = \sum_{\ell=k_1}^{k_2} \left(\frac{\partial \tilde{q}_{c_j}^{(n)}}{\partial \tilde{T}_{c_\ell}} + \frac{\partial \tilde{q}_{w_{\ell_2-j+k_1}}^{(n)}}{\partial \tilde{T}_{w_{\ell_2-\ell+k_1}}} \right) (\tilde{T}_{c_\ell} - \tilde{T}_{c_\ell}^{(0)}) + \sum_{\ell=k_3}^{k_4} \frac{\partial \tilde{q}_{c_j}^{(n)}}{\partial \tilde{T}_{c_\ell}} (\tilde{T}_{c_\ell} - \tilde{T}_{c_\ell}^{(0)}); \tag{64}$$

for $j = k_3, \ldots, k_4$,

$$\frac{q_s'}{q'} - \tilde{q}_{c_j}^{(n)(0)} - \tilde{q}_{w_{m_2-j+k_3}}^{(n)(0)} = \sum_{\ell=k_1}^{k_2} \frac{\partial \tilde{q}_{c_j}^{(n)}}{\partial \tilde{T}_{c_\ell}} (\tilde{T}_{c_\ell} - \tilde{T}_{c_\ell}^{(0)}) + \sum_{\ell=k_3}^{k_4} \left(\frac{\partial \tilde{q}_{c_j}^{(n)}}{\partial \tilde{T}_{c_\ell}} + \frac{\partial \tilde{q}_{t_{m_2-j+k_3}}^{(n)}}{\partial \tilde{T}_{t_{m_2-\ell+k_3}}} \right) (\tilde{T}_{c_\ell} - \tilde{T}_{c_\ell}^{(0)}). \tag{65}$$

Equations (64) and (65) form a system of linear algebraic equations for the matching temperature along the shear plane and the chip-tool interface.

4. RESULTS FROM BEM ANALYSES

As described in Section 2, the BEM algorithm is first verified against the well-known Jaeger solutions (Jaeger, 1942) for surface temperature of a semi-infinite domain with surface heating over a finite region. Steady-state turning operations are considered next. The particular processing conditions considered (Tay *et al.*, 1974; Stevenson *et al.*, 1983; Dawson and Malkin, 1984) are tabulated in Table 1. The geometric dimensions for these

Table 1. Processing conditions

Workpiece speed, v_s	0.5–2.5 m s^{-1}
Chip speed, v_c	0.23–1.15 m s^{-1}
Shear angle, ϕ	30°
Rake angle, α	20°
Clearance angle, θ	6°
Pe	1, 10, 20, 30, 40
Nu	0.003

Table 2. Dimensions in different regions

Workpiece:	L^*	12.0
	$L_\uparrow^*$	2.0
	W^*	5.0
Tool:	L_w^*	6.0
	L_t^*	10.0
Chip:	ℓ_c^*	$\cos(\phi-\alpha)$
	L_∞^*	10.0

calculations are tabulated in Table 2. In all the following cases, the thermophysical properties are assumed to be the same in all three regions. This assumption does not change the physics of the problem, but simplifies the numerical implementation. These calculations provide an indication of the speed and efficiency of the method. The boundaries of the workpiece, the chip and the tool are discretized into 62, 47 and 50 segments, respectively. The segments are divided in such a way that fine scales are used to resolve the high gradient region. The calculation was done on a Sun Microsystem 3/260. The CPU time for all cases was approximately 0.4 s.

The dimensionless surface temperatures $[Pe(T-T_\infty)k_w/q'\ell']$ along the primary shear plane for several different Peclet numbers ranging from 1 to 40 are plotted in Fig. 7(a). The abscissa is the dimensionless distance along the shear plane (see Fig. 3) measured from A ($x = 0$) to B ($x = 1$). It can be observed that the temperature increases gradually, attains a maximum, and decreases. For $Pe = 1$, the maxima occurs at $x = 0.64$. As the Peclet number increases, the location of the maxima shifts to the right and for $Pe = 40$, the maxima occurs at $x = 0.91$. Its magnitude also changes from 0.637 to 0.051 as the Peclet number goes from 1 to 40. The comparisons between the present BEM single-region results and those obtained by Dawson and Malkin (1984) using FEM are presented in Fig. 7(b). The Peclet number is 4.5 and the shear angle is 30°. For this case, the maximum discrepancy between the two is 15%. The BEM results obtained by matching all three regions are also plotted in Fig. 7(b). It can be observed that the interface temperature is considerably lower because of the fact that not all the heat generated in the primary zone is conducted into the workpiece.

The dimensionless temperatures along the chip-tool interface for five different Peclet numbers are plotted in Fig. 8. The abscissa is the dimensionless distance measured from B ($x = 0$) to C ($x = 1$) along the tool-chip interface (see Fig. 3). For $Pe = 1$, the maximum dimensionless temperature is 0.598 and occurs at $x = 0.1$. As the Peclet number increases, the temperature peak shifts to the right and for $Pe = 40$, a temperature peak of 0.087 occurs at $x = 0.5$. The maximum temperature is believed to be responsible for the crater wear in the tool.

Figure 9 presents the dimensionless heat flux along the shear plane going into the workpiece $[q^{(n)}_{\text{workpiece}}/q']$ for various Peclet numbers. The dimensionless heat flux is scaled by the heat generation in the shear plane. Conservation of energy requires that the sum of the fluxes going into the workpiece and the chip along the shear plane be equal to 1. It is interesting to note that in some parts of the shear plane the heat flux going to the workpiece is greater than one. This means that in addition to the heat generated within the shear plane, heat is conducted to the workpiece from the chip. This effect is more noticeable near the trailing edge (point B in Fig. 3). This is expected, since the secondary contact region (between the tool and the chip) is right next to it. The heat generated in the chip-tool contact region is dissipated into the chip and then to the workpiece. It is observed that this effect decreases as the Peclet number (i.e. the cutting speed) increases. As the cutting speed increases, the heat convected by the chip also increases. Consequently, less heat is dissipated into the workpiece.

The dimensionless heat fluxes along the chip-tool interface (B–C) going into the tool are plotted in Fig. 10. As mentioned before, it has been assumed (Tay *et al.*, 1974; Levy *et al.*, 1976; Stevenson *et al.*, 1983) that the total heat generation due to frictional heating and plastic deformation in the secondary zone is one-quarter of that in the primary zone.

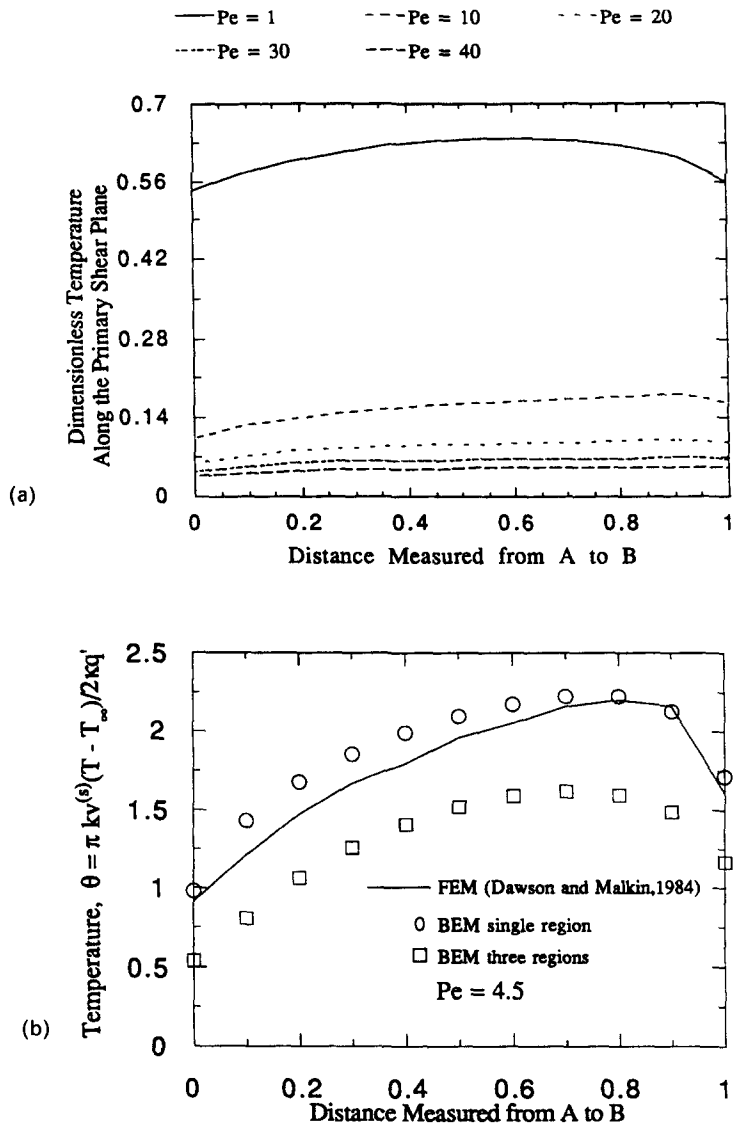

Fig. 7. Dimensionless temperature along the primary shear plane: (a) for different Peclet numbers and (b) comparisons of BEM and FEM results for $Pe = 4.5$.

The dashed curve labeled "ref" shows the total heat generation in the secondary zone, which is the sum of the heat fluxes going into the tool and the chip. It is assumed to be constant ($q_s'/q' = 2/9$) between $x = 0$ and $x = 0.5$ and to decrease linearly to 0 between $x = 0.5$ and $x = 1$. Figure 10 also presents the proportion of the total flux going into the tool and the chip for different Peclet numbers. The vertical distance between an appropriate curve and the horizontal line for $\tilde{q} = 0$ represents the magnitude of the flux going into the tool, while the vertical distance between the appropriate curve and the "ref" curve represents that going into the chip at any value of x. In all the cases considered, it has been observed that more heat is dissipated into the chip than into the tool.

The variation of the distribution of the total heat flux (primary and secondary) dissipated into the chip, the tool and the workpiece with respect to the Peclet number is plotted in Fig. 11. At $Pe = 1$, about 25% of the total heat generated is carried into the chip, while about 50% goes into the workpiece. As the Peclet number increases, the portion of the heat carried by the chip increases rapidly. For $Pe = 50$, about 90% of the heat generated dissipates through the chip, while only 4% goes to the workpiece.

A schematic diagram for a machining process with flank wear is shown in Fig. 12. Figures 13 and 14 show the temperature and flux fields, respectively, along the primary

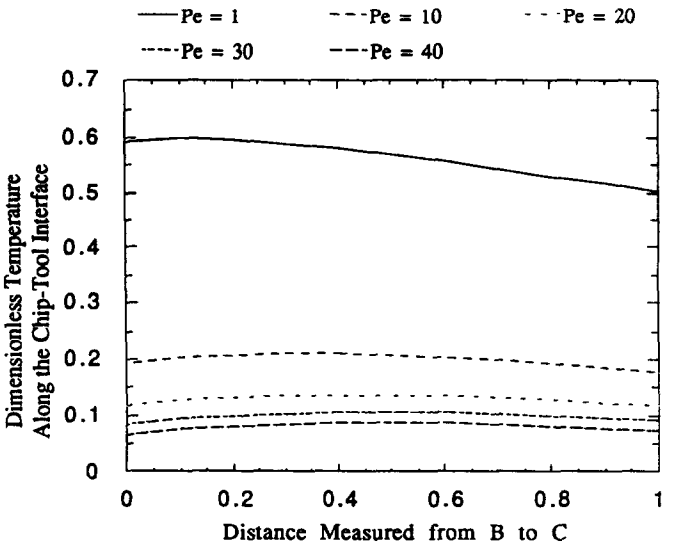

Fig. 8. Dimensionless temperature along the contact surface for different Peclet numbers ($\phi = 30°$, $\alpha = 20°$, $\theta = 5°$).

shear plane, secondary chip-tool interface, and the tool-workpiece or flank wear interface. The processing conditions are shown in Table 3. The dimensionless interface temperatures along the primary shear plane (A–B) and the flank wear region (B–D) are plotted in Fig. 13(a). The temperature increases to a maximum of $\tilde{T}$ ($\tilde{T} = Pe(T - T_\infty)k_w/q'_\ell$) equal to 0.21 near point B and then decreases gradually to $\tilde{T} = 0.17$ at point D. Figure 13(b) shows the variation of $\tilde{T}$ along the chip-tool interface (C–B). $\tilde{T}$ reaches a peak value of 0.24 at about the midpoint of CB. These temperature distributions are as expected for machining problems and, qualitatively, compare well with the earlier results of Dawson and Malkin (1984) and Chan and Chandra (1991a).

Figure 14 shows the dimensionless heat flux ($\tilde{q} = q^{(n)}/q'$) along the workpiece-chip, workpiece-tool, and chip-tool interfaces. The conservation of energy requires that the heat generation be balanced by the fluxes. It is interesting to note that, in some parts of the shear

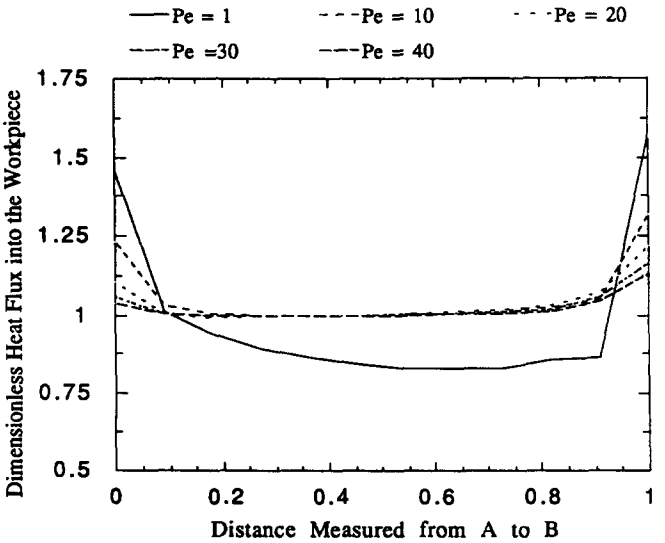

Fig. 9. Dimensionless heat flux in the workpiece along the shear plane for different Peclet numbers ($\phi = 30°$, $\alpha = 20°$, $\theta = 5°$).

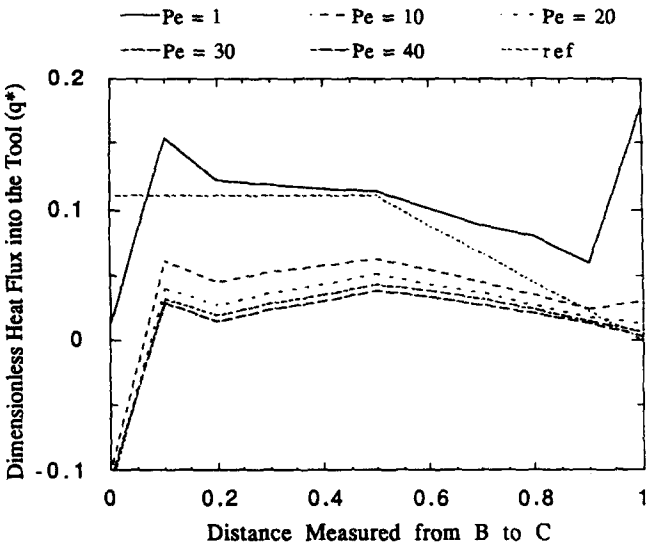

Fig. 10. Dimensionless heat flux in the tool along the contact surface for different Peclet numbers ($\phi = 30°$, $\alpha = 20°$, $\theta = 5°$).

plane, the heat flux going to the workpiece is greater than one. This implies that, in addition to the heat generated within the shear plane, heat is conducted to the workpiece from the chip. Similar effects are also observed along the chip-tool interface near points C and B. Along the workpiece-tool interface, $\tilde{q}$ is negative. This implies heat conduction from the tool to the workpiece.

5. BEM SENSITIVITY FORMULATION

As discussed earlier, the governing equation for temperature distributions in each of the regions (tool, chip and workpiece) in steady-state machining operations may be expressed as (Chan and Chandra, 1991c)

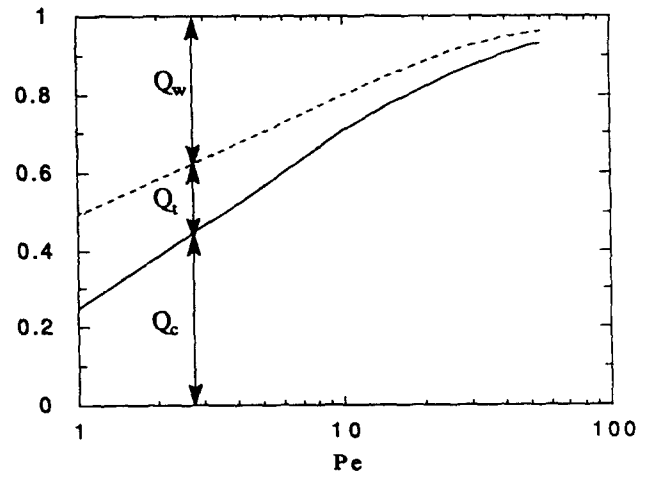

Fig. 11. Distribution of the total heat generation dissipated into the chip, the tool and the workpiece. Q_c, Q_t, and Q_w are the fractions for the chip, the tool and the workpiece, respectively.

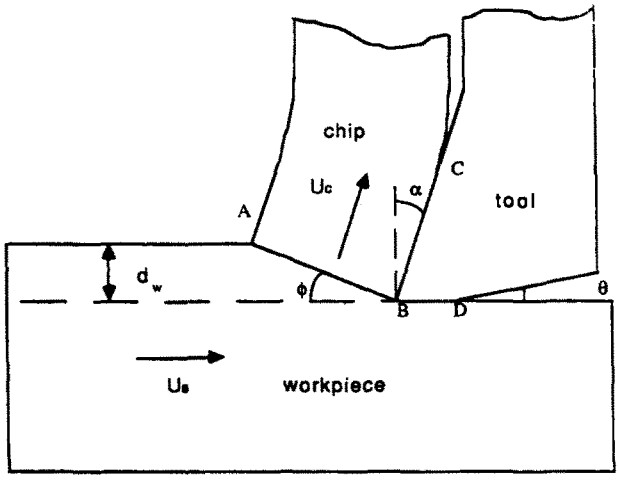

Fig. 12. Schematic diagram of orthogonal cutting.

$$-k\frac{\partial^2 T}{\partial x_i^2}+\rho c v_i^{(s)}\frac{\partial T}{\partial x_i}=0 \quad \text{in} \quad B. \tag{66}$$

Here $v_i^{(s)}$ is the convective velocity in that region and $\kappa = k/\rho c$ is the thermal diffusivity.

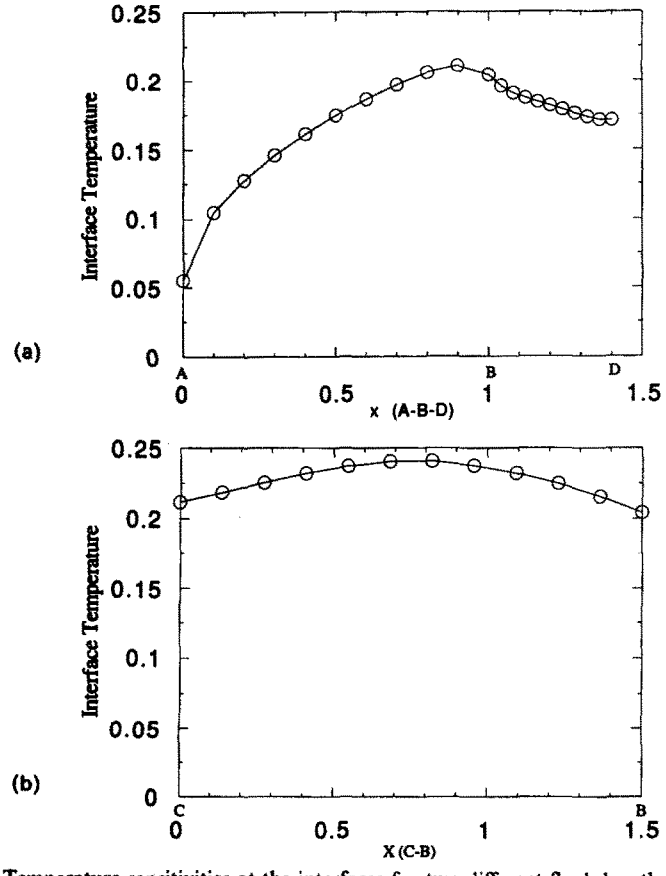

Fig. 13. Temperature sensitivities at the interfaces for two different flank lengths: (a) workpiece-chip (AB) and workpiece-tool (BD) interfaces and (b) chip-tool interface (CB).

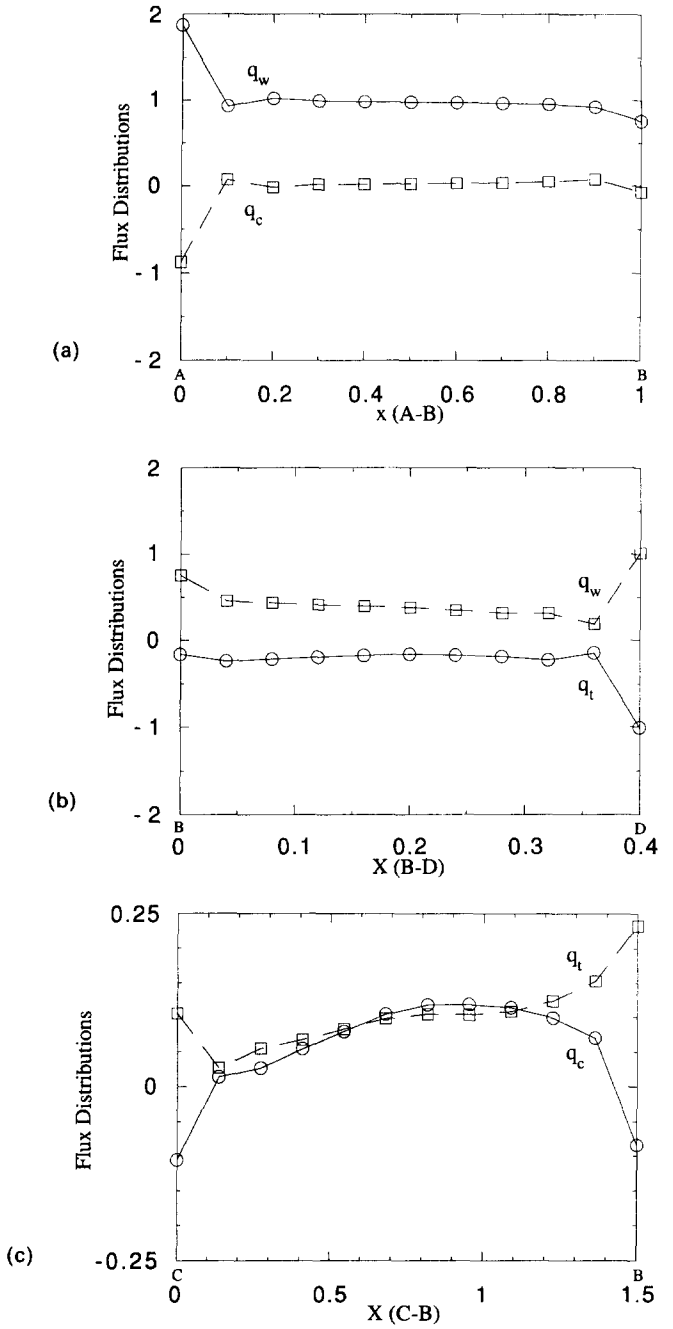

Fig. 14. Flux sensitivities at the interfaces for two different flank lengths: (a) workpiece-chip (AB) interface, (b) workpiece-tool (BD) interface, and (c) chip-tool (CB) interface.

Table 3. Processing conditions

Shear angle, ϕ	5°
Rake angle, α	20°
Clearance angle, θ	6°
Flank land	0.4 × shear plane length
Pe	18
Nu	0.003

The boundary conditions may be expressed as

$$T = \bar{T} \qquad \text{on} \quad \partial B_T \tag{66a}$$

and

$$k\frac{\partial T}{\partial x_i}n_i = \bar{q} \qquad \text{on} \quad \partial B_q \tag{66b}$$

or

$$k\frac{\partial T}{\partial x_i}n_i = h(T - T_\infty) \quad \text{on} \quad \partial B_h. \tag{66c}$$

Here, T represents the temperature field, q represents the flux, k is the thermal conductivity of the material, h is the convection coefficient, T_∞ represents the ambient temperature, x_i represents the spatial coordinates, and n_is are the components of the outward normal on the boundary of the domain. Equation (66) applies to a Eulerian reference frame that remains spatially fixed while the material flows through it. The convective term represents the energy transported by the material as it moves through the reference frame. Following Tanaka *et al.* (1986) and Chan and Chandra (1991a), an integral equation for an internal point may be written as

$$T(p) = \int_{\partial B} \left\{ -\left[k\frac{\partial G(p,Q)}{\partial n_Q} + \rho c G(p,Q) v_i^{(s)} n_i(Q) \right] T(Q) + kG(p,Q) q^{(n)}(Q) \right\} \mathrm{d}s(Q), \tag{67a}$$

when

$$v_{i,i}^{(s)} = 0. \tag{67b}$$

Here, a comma denotes field point differentiation; p and q represent a source point and a field point, respectively, in the domain; and P and Q represent a source point and a field point on the boundary. $G(p,q)$ is the Green's function for the steady-state conduction–convection eqn (66). For two- or three-dimensional applications, appropriate versions of the fundamental solution $G(p,q)$ should be used. These are available in several references (Tanaka *et al.*, 1986; Chan and Chandra, 1991a). In the present work, the numerical implementation of the BEM formulation is done in two-dimensional situations only. Hence, two-dimensional versions of the above equations are presented in this section. The BEM formulation, however, is also valid for three-dimensional situations.

A boundary integral equation for the steady-state conduction–convection problem may now be obtained as $p \to P$ (Chan and Chandra, 1991a). This gives

$$C(P)T(P) = \int_{\partial B} \left\{ -\left[k\frac{\partial G(P,Q)}{\partial n_Q} + \rho c G(P,Q) v_i^{(s)} n_i(Q) \right] T(Q) + kG(P,Q) q^{(n)}(Q) \right\} \mathrm{d}s(Q). \tag{68}$$

The coefficient $C(P)$, called the "corner tensor", depends upon the local geometry at P. If the boundary is locally smooth at P, $C = 1/2$. Otherwise, it may be evaluated indirectly (Tanaka *et al.*, 1986; Chan and Chandra, 1991a) as shown below.

By applying a unit temperature field all over the boundary of the body, it may be shown that

$$C(P) = \int_{\partial B} -\left[k\frac{\partial G(P,Q)}{\partial n_Q} + \rho c G(P,Q) v_i^{(s)} n_i(Q) \right] \mathrm{d}s(Q). \tag{69}$$

Substituting eqn (69) in eqn (68), we get

$$0 = \int_{\partial B} \left\{ -\left[k\frac{\partial G(P,Q)}{\partial n_Q} + \rho c G(P,Q)\mathbf{v}_i^{(s)} n_i(Q) \right][T(Q) - T(P)] \right.$$
$$\left. + kG(P,Q)q^{(n)}(Q) \right\} \mathrm{d}s(Q). \quad (70)$$

In order to determine the design sensitivities of temperature and flux with respect to any design parameter, eqn (70) may be differentiated with respect to the particular parameter of interest. Barone and Yang (1988) and Mukherjee and Chandra (1989, 1991) have investigated shape optimization and assumed at this stage that the shape of a body is determined by a finite dimensional vector with components b_i and that the shape changes occur continuously. The design parameters b_i, however, need not be restricted to shape variables. Process parameters like the scanning velocity, material parameters like thermal diffusivity, or a combined parameter like the Peclet number may also be chosen as the design parameter of interest. It is also possible to choose the specified boundary conditions as design parameters. Differentiating eqn (70) with respect to a typical b_i (designated here as a shape parameter, b), we get (Chandra and Chan, 1992)

$$0 = \int_{\partial B} \left\{ -\left[k\frac{\partial G(b,P,Q)}{\partial n_Q} + \rho c G(b,P,Q)\mathbf{v}_i^{(s)}(b) n_i(b,Q) \right][\overset{*}{T}(b,Q) - \overset{*}{T}(b,P)] \right.$$
$$\left. + kG(b,P,Q)\overset{*}{q}^{(n)}(b,Q) \right\} \mathrm{d}s(b,Q) + \int_{\partial B} \left\{ -\left[k\frac{\partial \overset{*}{G}(b,P,Q)}{\partial n_Q} \right.\right.$$
$$\left. + \rho c\overset{*}{G}(b,P,Q)\mathbf{v}_i^{(s)}(b) n_i(b,Q) + \rho c G(b,P,Q)\mathbf{v}_i^{(s)}(b)\overset{*}{n}_i(b,Q) \right]$$
$$\times [T(b,Q) - T(b,P)] + k\overset{*}{G}(b,P,Q)q^{(n)}(b,Q) \Big\} \mathrm{d}s(b,Q)$$
$$+ \int_{\partial B} \left\{ -\left[k\frac{\partial G(b,P,Q)}{\partial n_Q} + \rho c G(b,P,Q)\mathbf{v}_i^{(s)}(b) n_i(b,Q) \right][T(b,Q) - T(b,P)] \right.$$
$$\left. + kG(b,P,Q)q^{(n)}(b,Q) \right\} \mathrm{d}\overset{*}{s}(b,Q), \quad (71)$$

where a superposed asterisk (*) denotes a derivative with respect to b. Other types of parameters such as process parameters (e.g. cutting velocity) and material parameters (e.g. thermal conductivity, specific heat) may also be chosen as design variables. In such cases, appropriate sensitivity equations including the requisite additional terms may be derived easily following the same procedure outlined above.

The kernels $\overset{*}{G}(b,P,Q)$ and $[\partial \overset{*}{G}(b,P,Q)]/\partial n_Q$ may be expressed as (Barone and Yang, 1988; Mukherjee and Chandra, 1989, 1991)

$$\overset{*}{G}(b,P,Q) = G_{,k}(b,P,Q)[\overset{*}{x}_k(Q) - \overset{*}{x}_k(P)], \quad (72)$$

$$\frac{\partial \overset{*}{G}(b,P,Q)}{\partial n_Q} = \frac{\partial G_{,k}(b,P,Q)}{\partial n_Q}[\overset{*}{x}_k(Q) - \overset{*}{x}_k(P)] + \overset{*}{n}_k(Q)G_{,k}(b,P,Q) \quad (73)$$

and

$$\mathrm{d}\overset{*}{s}(b,Q)=\left\{\frac{\dfrac{\partial}{\partial b}\left(\left|\dfrac{\partial}{\partial\eta}(x_k e_k)\right|\right)}{\left|\dfrac{\partial}{\partial\eta}(x_k e_k)\right|}\right\}\mathrm{d}s(b,Q), \tag{74}$$

where b is a shape parameter and e_k represents a component of a unit vector. The quantity $[\overset{*}{x}_k(Q)-\overset{*}{x}_k(P)]\sim O(r)$. Hence, when b is a shape parameter, $\overset{*}{G}$ and $\partial\overset{*}{G}/\partial n_Q$ are regular and $1/r$ singular, respectively, for two-dimensional applications. When b is not a shape parameter, $\mathrm{d}\overset{*}{s}$ is zero. It can be seen that differentiation with respect to a non-spatial variable does not affect the order of singularity in either G or $\partial G/\partial n_Q$.

Once the standard BEM analysis is performed, the temperature $T(b,Q)$ and the flux $q^{(n)}(b,Q)$ are known everywhere on the boundary. From the given boundary conditions, half of the quantities of $\overset{*}{T}(b,Q)$ and $\overset{*}{q}^{(n)}(b,Q)$ are known for a well-posed problem. Hence, eqns (71)–(74) may be used to solve for the unknown temperature sensitivities and flux sensitivities on the boundary in terms of the known ones.

A sensitivity equation for an internal point may now be obtained by differentiating eqn (67a) with respect to b. This gives,

$$\begin{aligned}\overset{*}{T}(b,p)=&\int_{\partial B}\left\{-\left[k\frac{\partial G(b,p,Q)}{\partial n_Q}+\rho cG(b,p,Q)\mathrm{v}_i^{(s)}(b)n_i(b,Q)\right]\overset{*}{T}(b,Q)\right.\\&\left.+kG(b,p,Q)\overset{*}{q}^{(n)}(b,Q)\right\}\mathrm{d}s(b,Q)+\int_{\partial B}\left\{-\left[k\frac{\partial\overset{*}{G}(b,p,Q)}{\partial n_Q}\right.\right.\\&\left.+\rho c\overset{*}{G}(b,p,Q)\mathrm{v}_i^{(s)}(b)n_i(b,Q)+\rho cG(b,p,Q)\mathrm{v}_i^{(s)}(b)\overset{*}{n}_i(b,Q)\right]T(b,Q)\\&\left.+k\overset{*}{G}(b,p,Q)q^{(n)}(b,Q)\right\}\mathrm{d}s(b,Q)+\int_{\partial B}\left\{-\left[k\frac{\partial G(b,p,Q)}{\partial n_Q}\right.\right.\\&\left.\left.+\rho cG(b,p,Q)\mathrm{v}_i^{(s)}(b)n_i(b,Q)\right]T(b,Q)+kG(b,p,Q)q^{(n)}(b,Q)\right\}\mathrm{d}\overset{*}{s}(b,Q).\end{aligned} \tag{75}$$

It should be noted here that eqn (75) requires only algebraic evaluations for the determination of $\overset{*}{T}(b,p)$. The kernels, in this case, do not become singular since Q lies on the boundary, while p is strictly an interior point.

Numerical implementation of the BEM eqns (68), (71)–(74) for heat transfer and design sensitivities in conduction–convection problems is discussed in this section. In the present work, two-dimensional problems are considered.

The first step is the discretization of the boundary of the two-dimensional domain into boundary elements. A discretized version of the standard boundary integral equation may be written as

$$\begin{aligned}C(P_M)T(P_M)=&-\sum_{i=1}^{N_s}\left\{\int_{\Delta S_i}k\frac{\partial G(P_M,Q)}{\partial n_Q}T(Q)-kG(P_M,Q)q^{(n)}(Q)\right\}\mathrm{d}s(b,Q)\\&-\sum_{i=1}^{N_s}\int_{\Delta S_i}\rho cG(P_M,Q)T(Q)v_\ell^{(s)}n_\ell(Q)\,\mathrm{d}s(b,Q).\end{aligned} \tag{76}$$

A discretized BEM sensitivity equation may also be written as

$$0 = \sum_{i=1}^{N_s} \int_{\Delta s_i} \left\{ -\left[k \frac{\partial G(b, P_M, Q)}{\partial n_Q} + \rho c G(b, P, Q) v_\ell^{(s)}(b, Q) n_\ell(b, Q) \right] \right.$$

$$\left. \times [\overset{*}{T}(b, Q) - \overset{*}{T}(b, P_M)] + k G(b, P_M, Q) \overset{*}{q}^{(n)}(b, Q) \right\} \mathrm{d}s(Q)$$

$$+ \sum_{i=1}^{N_s} \int_{\Delta s_i} \left\{ -\left[k \frac{\partial \overset{*}{G}(b, P_M, Q)}{\partial n_Q} + \rho c \overset{*}{G}(b, P, Q) v_\ell^{(s)}(b) n_\ell(b, Q) \right.\right.$$

$$\left. + \rho c G(b, P_M, Q) v_\ell^{(s)}(b) \overset{*}{n}_\ell(b, Q) \right] [T(b, Q) - T(b, P)]$$

$$\left. + k \overset{*}{G}(b, P_M, Q) q^{(n)}(b, Q) \right\} \mathrm{d}s(b, Q) + \sum_{i=1}^{N_s} \int_{\Delta s_i} \left\{ -\left[k \frac{\partial G(b, P_M, Q)}{\partial n_Q} \right.\right.$$

$$\left. + \rho c G(b, P_M, Q) v_\ell^{(s)}(b) n_\ell(b, Q) \right] [T(b, Q) - T(b, P_M)]$$

$$\left. + k G(b, P_M, Q) q^{(n)}(b, Q) \right\} \mathrm{d}\overset{*}{s}(b, Q), \tag{77}$$

where the boundary of the domain ∂B is divided into N_s boundary segments and $T(P_M)$ represents temperature at a point P that coincides with node M.

Suitable shape functions must now be chosen for the variation of temperature, temperature sensitivity, flux, and flux sensitivity over each boundary element Δs_i. In the present work, each of the above quantities is assumed to vary linearly over individual boundary elements. A matrix equation for the standard BEM eqn (76) may be derived as (details in Chan and Chandra, 1991b)

$$\sum_{j=1}^{N_s} A_{ij} T_j = \sum_{j=1}^{N_s} (b_{ij-1}^{(2)} q_j^{(n)} + b_{ij}^{(1)} q_j^{(n)'}). \tag{78}$$

Here, $q_j^{(n)}$ is the flux at the jth node in the normal direction of the element just before the node, while $q_j^{(n)'}$ is the flux at the jth node in the normal direction of the element just after the node. When the surface is smooth at the jth node, $q_j^{(n)}$ and $q_j^{(n)'}$ are equal to one another. By splitting up the normal flux, a geometrical corner can be handled properly (Chan and Chandra, 1991b). A_{ij} represents an element of the assembled matrix that multiplies T_j, where $b_{ij-1}^{(2)}$ and $b_{ij}^{(1)}$ refer to the contributions from the second node of the $(j-1)$th segment and the first node of the jth segment, respectively, for the matrix multiplying the normal flux. This allows proper modeling of the jump in the normal flux across a geometric corner.

Similarly, a matrix equation for the design sensitivity eqn (77) may be derived as

$$\sum_{j=1}^{N_s} A_{ij} \overset{*}{T}_j - \sum_{j=1}^{N_s} (b_{ij-1}^{(2)} \overset{*}{q}_j^{(n)} + b_{ij}^{(1)} \overset{*}{q}_j^{(n)'}) = -\sum_{j=1}^{N_s} \overset{*}{A}_{ij} T_j + \sum_{j=1}^{N_s} (\overset{*}{b}_{ij-1}^{(2)} q_j^{(n)} + \overset{*}{b}_{ij}^{(1)} q_j^{(n)'}). \tag{79}$$

It is clear from eqn (79) that eqn (78) should be solved first. Once temperature and flux are known everywhere on the boundary, eqn (79) can be solved for the design sensitivities. It should be noted that the coefficient matrices A_{ij}, $b_{ij-1}^{(2)}$, and $b_{ij}^{(1)}$ appearing in eqn (79) are exactly the same as those in eqn (78).

At each location over the entire boundary of the domain, either $T(\overset{*}{T})$ or $q^{(n)}(\overset{*}{q}^{(n)})$ (or a combination of the two) is prescribed for a well-posed problem. Equation (78) may now be solved for the unknown T and $q^{(n)}$ in terms of the known ones. Using these results, eqn (79) may be solved for the unknown sensitivities $\overset{*}{T}$ and $\overset{*}{q}^{(n)}$ (or $\overset{*}{q}^{(n)'}$ as appropriate). Typically, the temperature or the flux sensitivity is zero when the temperature or the flux

is specified, respectively, at any particular point on the boundary. It should be noted that the BEM sensitivity formulation can also accommodate any arbitrarily specified $\overset{*}{T}$ or $\overset{*}{q}$ on any portion of the boundary. Once $\overset{*}{T}$ and $\overset{*}{q}$ have been obtained over the entire boundary, the internal eqn (75) may be used to obtain the temperature sensitivity at any internal point. A derivative form of the eqn (75) may also be used to determine the flux sensitivity at any internal point.

It is also important to note here that the matrices A_{ij} and B_{ij} in eqn (77) depend on the reference configuration only and do not depend on the choice of the design parameter b. All the effects for a particular choice of b are incorporated through the right-hand side vector $\mathbf{F}_i$ in eqn (77). This makes the BEM formulation very efficient when sensitivities with respect to a (relatively) large number of design variables are sought for a particular reference configuration. For the small increase in additional costs due to additional evaluations of the right-hand side, sensitivities with respect to several design variables may be obtained. Using parallel processing features, such design sensitivities may also be tracked simultaneously.

6. SENSITIVITIES OF MACHINING PROCESSES

In this section, the BEM sensitivity formulation is used to model a steady-state machining process. A schematic diagram of the process is sketched in Fig. 3. Typically, the tool is a large-angled wedge that is driven into the workpiece to remove a thin layer, the chip. As the tool is driven into the workpiece, the material undergoes a severe plastic deformation along the shear plane. As the chip forms, it diverts and slides across the tool face. The tool also wears out as the machining continues. There are three main sources of heat generation: (1) the heat generated by the plastic deformation in the shear plane, (2) the frictional heating and plastic deformation as the chip slides over the tool face, and (3) the frictional heating and plastic deformation due to the flank wear of the tool at the tool-workpiece interface. The heat transfer involved here is conduction and convection of the heat generated into the tool, the chip and the workpiece.

In a machining operation, the velocities associated with the tool, the workpiece, and the chip are quite different. Fixing the reference frame to the tool, it may be considered stationary. The workpiece, with respect to such a reference frame, moves at the cutting velocity (scanning velocity). The chip moves in a different direction with a velocity related to the scanning and the shear plane angle. Therefore, the algorithm is applied to each region separately. For oblique cutting, the BEM algorithm is applied separately to each of the regions because the chip velocity may also depend on the tool angles. By matching the boundary conditions at the workpiece-chip interface, the workpiece-tool interface, and the chip-tool interface, a complete solution for the machining problem may then be obtained. Orthogonal machining is considered here, and two-dimensional analyses of heat transfer and their sensitivities are performed. In order to model the heat transfer efficiently, the tool, the chip and the workpiece are formulated separately. Furthermore, a coordinate system unique to each region is defined in order to better represent the boundary elements. The coordinate systems for the three regions are defined in Fig. 12.

6.1. *Matching boundary conditions for sensitivity calculations*

The matching boundary conditions along the shear plane, the chip-tool interface, and the tool-workpiece interface are now presented. Along the shear plane, often referred to as the primary deformation zone, heat is generated as a result of the large plastic deformation. Assuming that the rate of work in the deformation zone is converted entirely into heat, the heat generation can be calculated by the following equation (Tay *et al.*, 1974; Stevenson *et al.*, 1983; Dawson and Malkin, 1984)

$$q'\delta_{sp} = \tau\dot{\gamma}, \tag{80}$$

where q' is the volumetric heat generation, τ is the yield stress, and $\dot{\gamma}$ is the shear strain rate which can be calculated from

$$\dot{\gamma} = \frac{CV_{\text{slide}}}{d_w} = \frac{C}{d_w} \frac{v_s \cos \alpha}{\cos (\phi - \alpha)} \tag{81}$$

where C is an empirical constant, V_{slide} is the sliding velocity that is related to the scanning velocity v_s, the rake angle α, and the shear plane angle ϕ. δ_{sp} is a Dirac delta function situated along the shear plane. Consequently, the heat generated is assumed to be concentrated along the shear plane. Applying an energy balance along the shear plane, the matching boundary condition can be obtained:

$$q^{(n)}_{\text{workpiece}} + q^{(n)}_{\text{chip}} = q'. \tag{82}$$

Furthermore, the continuity of temperature is also prescribed,

$$T_w = T_c. \tag{83}$$

The matching boundary conditions for the sensitivities can be obtained by differentiating the above equations:

$$\overset{*}{q}{}^{(n)}_{\text{workpiece}} + \overset{*}{q}{}^{(n)}_{\text{chip}} = \overset{*}{q}{}', \tag{84}$$

$$\overset{*}{T}_w = \overset{*}{T}_c. \tag{85}$$

If the heat generation in the shear plane is unaffected by the design parameter b, then $\overset{*}{q}{}'$ is equal to zero.

The secondary deformation zone is located along the chip-tool interface. Heat is generated by plastic deformation and frictional heating. Here, both effects are modeled by a total volumetric heat generation $q'_s \delta_{ct}$ concentrated along the chip-tool interface. Once again, applying the energy balance, the matching condition along the chip-tool interface is

$$q^{(n)}_{\text{chip}} + q^{(n)}_{\text{tool}} = q'_s \tag{86}$$

and

$$T_c = T_t. \tag{87}$$

The matching conditions for the sensitivities are

$$\overset{*}{q}{}^{(n)}_c + \overset{*}{q}{}^{(n)}_{\text{tool}} = \overset{*}{q}{}'_s, \tag{88}$$

$$\overset{*}{T}_c = \overset{*}{T}_t. \tag{89}$$

For crater wear, the matching boundary conditions are given by eqns (86)–(89).

In the case of flank wear, there is a third deformation zone located along the workpiece-tool interface. Heat is generated by plastic deformation and frictional heating. Here, both effects are modeled by a total volumetric heat generation $q'_F \delta_{wt}$ concentrated along the workpiece-tool interface. The matching boundary conditions are

$$q^{(n)}_w + q^{(n)}_t = q'_F, \tag{90}$$

$$T_w = T_t, \tag{91}$$

and

$$\overset{*}{q}_w^{(n)} + \overset{*}{q}_t^{(n)} = \overset{*}{q}_F', \tag{92}$$

$$\overset{*}{T}_w = \overset{*}{T}_t. \tag{93}$$

6.2. *Matching scheme for the sensitivity problem*

As mentioned before, the BEM algorithm is first applied to solve the heat transfer in each region separately. By matching the sensitivity boundary conditions along the shear plane, the chip-tool interface, and the workpiece-tool interface, a complete solution may then be obtained. Starting from an initial solution, an exact expression can be derived to satisfy the matching conditions without iterations. A detailed description can be found in Chan and Chandra (1991c). This matching scheme will now be briefly presented. A schematic diagram of the matching is shown in Fig. 3.

Applying the BEM sensitivity algorithm to each region, the following matrix equations may be obtained (Chan and Chandra, 1991a, b):

$$\sum_{j=1}^{N_s} A_{ij} \overset{*}{T}_j = \sum_{j=1}^{N_s} (b_{ij-1}^{(2)} \overset{*}{q}_j^{(n)} + b_{ij}^{(1)} \overset{*}{q}_j^{(n)'}). \tag{94}$$

A switching process is applied by keeping the unknown quantities on the left-hand side and the known quantities on the right-hand side (Chan and Chandra, 1991b).

Along a matching interface, the heat flux is treated as an unknown and the temperature is treated as a known variable. Taking the derivative of the matrix equation with respect to a node temperature along an interface ($\overset{*}{Y}_j^{(n)}$ is the unknown sensitivity variable at the jth node after switching),

$$\sum_{j=1}^{N_s} \tilde{A}_{ij} \frac{\partial \overset{*}{Y}_j^{(u)}}{\partial \overset{*}{T}_\ell} = \tilde{B}_{i\ell}. \tag{95}$$

All the derivatives are independent of temperature and flux. Consequently, an exact linear equation can be derived as

$$\overset{*}{q}_j^{(n)} - \overset{*}{q}_j^{(n)(0)} = \sum_{\ell=\ell_1}^{\ell_2} (\overset{*}{T}_\ell - \overset{*}{T}_\ell^{(0)}) \frac{\partial \overset{*}{q}_j^{(n)}}{\partial \overset{*}{T}_\ell}. \tag{96}$$

Here, $\overset{*}{q}_j^{(n)(0)}$ is the solution of eqn (94) based on an arbitrarily prescribed $\overset{*}{T}_\ell^{(0)}$. On a node along the matching interface, two equations (one from each region) may be derived. Using the two matching boundary conditions [e.g. eqns (82)–(83)], the heat flux may be eliminated to obtain an equation with temperature being the unknown. Applying this to each node along the interface, a matrix equation can be obtained for the matching interface temperatures:

for the workpiece-chip interface, $\ell_1 \leqslant \ell < \ell_2$,

$$\overset{*}{q}' - \overset{*}{q}_{w_\ell}^{(n)(0)} - \overset{*}{q}_{c_{k_3-(\ell-\ell_2)}}^{(n)(0)} = \sum_{j=\ell_1}^{\ell_2} \left(\frac{\partial \overset{*}{q}_{w_\ell}^{(n)}}{\partial \overset{*}{T}_{w_j}} + \frac{\partial \overset{*}{q}_{c_{k_3-(\ell-\ell_2)}}}{\partial \overset{*}{T}_{c_{k_3-(j-\ell_2)}}} \right) (\overset{*}{T}_{w_j} - \overset{*}{T}_{w_j}^{(0)})$$

$$+ \sum_{j=\ell_2+1}^{\ell_3} \frac{\partial \overset{*}{q}_{w_\ell}^{(n)}}{\partial \overset{*}{T}_{w_j}} (\overset{*}{T}_{w_j} - \overset{*}{T}_{w_j}^{(0)}) + \sum_{j=k_1}^{k_2-1} \frac{\partial \overset{*}{q}_{c_{k_3-(\ell-\ell_2)}}}{\partial \overset{*}{T}_{c_j}} (\overset{*}{T}_{c_j} - \overset{*}{T}_{c_j}^{(0)}); \tag{97}$$

for the workpiece-tool interface, $\ell_2 < \ell \leqslant \ell_3$,

$$\dot{q}'_F - \dot{q}^{(n)(0)}_{w_\ell} - \dot{q}^{(n)(0)}_{t_{m_2-(\ell-\ell_2)}} = \sum_{j=\ell_1}^{\ell_2-1} \frac{\partial \dot{q}^{(n)}_{w_\ell}}{\partial \dot{T}_{w_j}} \left(\dot{T}_{w_j} - \dot{T}^{(0)}_{w_j}\right) + \sum_{j=\ell_2}^{\ell_3} \frac{\partial \dot{q}^{(n)}_{w_\ell}}{\partial \dot{T}_{w_j}}$$

$$+ \left(\frac{\partial \dot{q}_{t_{m_2-(\ell-\ell_2)}}}{\partial \dot{T}_{t_{m_2-(j-\ell_2)}}}\right)\left(\dot{T}_{w_j} - \dot{T}^{(0)}_{w_j}\right) + \sum_{j=k_1}^{k_2-1} \frac{\partial \dot{q}_{t_{m_2-(\ell-\ell_2)}}}{\partial \dot{T}_{t_{m_2-(j-k_1)}}} \left(\dot{T}_{c_j} - \dot{T}^{(0)}_{c_j}\right); \quad (98)$$

for the chip-tool interface, $k_1 \leqslant k < k_2$,

$$\dot{q}'_s - \dot{q}^{(n)(0)}_{c_k} - \dot{q}^{(n)(0)}_{t_{m_2-(k-k_1)}} = \sum_{j=\ell_1}^{\ell_2-1} \frac{\partial \dot{q}^{(n)}_{c_k}}{\partial \dot{T}_{w_{k_3-(j-\ell_1)}}} \left(\dot{T}_{w_j} - \dot{T}^{(0)}_{w_j}\right)$$

$$+ \left(\frac{\partial \dot{q}_{c_k}}{\partial \dot{T}_{c_{k_2}}} + \frac{\partial \dot{q}_{t_{m_2-(k-k_2)}}}{\partial \dot{T}_{t_{m_2}}}\right)\left(\dot{T}_{w_{\ell_2}} - \dot{T}^{(0)}_{w_{\ell_2}}\right) + \sum_{j=\ell_2+1}^{\ell_3} \frac{\partial \dot{q}_{t_{m_2-(k-k_1)}}}{\partial \dot{T}_{t_{m_2-(j-\ell_2)}}} \left(\dot{T}_{w_j} - \dot{T}^{(0)}_{w_j}\right)$$

$$+ \sum_{j=k_1}^{k_2-1} \left(\frac{\partial \dot{q}_{c_k}}{\partial \dot{T}_{c_j}} + \frac{\partial \dot{q}_{t_{m_2-(\ell-\ell_2)}}}{\partial \dot{T}_{t_{m_2-(j-k_1)}}}\right)\left(\dot{T}_{c_j} - \dot{T}^{(0)}_{c_j}\right). \quad (99)$$

At the node where all three regions meet,

$$\dot{q} + \dot{q}'_s + \dot{q}'_F - \dot{q}^{(n)(0)}_{w_{\ell_2}} - \dot{q}^{(n)(0)'}_{w_{\ell_2}} - \dot{q}^{(n)(0)}_{c_{k_2}} - \dot{q}^{(n)(0)'}_{c_{k_2}} - \dot{q}^{(n)(0)}_{t_{m_2}} - \dot{q}^{(n)(0)'}_{t_{m_2}}$$

$$= \sum_{j=\ell_1}^{\ell_2-2} \left(\frac{\partial \dot{q}^{(n)}_{w_{\ell_2}}}{\partial \dot{T}_{w_j}} + \frac{\partial \dot{q}^{(n)}_{c_{k_2}}}{\partial \dot{T}_{c_{k_3-(j+\ell_1)}}}\right)\left(\dot{T}_{w_j} - \dot{T}^{(0)}_{w_j}\right)$$

$$+ \left(\frac{\partial \dot{q}^{(n)}_{w_{\ell_2}}}{\partial \dot{T}_{w_{\ell_2-1}}} + \frac{\partial \dot{q}^{(n)'}_{w_{\ell_2}}}{\partial \dot{T}_{w_{\ell_2-1}}} + \frac{\partial \dot{q}^{(n)}_{c_{k_2}}}{\partial \dot{T}_{c_{k_2+1}}} + \frac{\partial \dot{q}^{(n)'}_{c_{k_2}}}{\partial \dot{T}_{c_{k_2+1}}}\right)\left(\dot{T}_{w_{\ell_2-1}} - \dot{T}^{(0)}_{w_{\ell_2-1}}\right)$$

$$+ \left(\frac{\partial \dot{q}^{(n)}_{w_{\ell_2}}}{\partial \dot{T}_{w_{\ell_2}}} + \frac{\partial \dot{q}^{(n)'}_{w_{\ell_2}}}{\partial \dot{T}_{w_{\ell_2}}} + \frac{\partial \dot{q}^{(n)}_{c_{k_2}}}{\partial \dot{T}_{c_{k_2}}} + \frac{\partial \dot{q}^{(n)'}_{c_{k_2}}}{\partial \dot{T}_{c_{k_2}}} + \frac{\partial \dot{q}^{(n)}_{t_{m_2}}}{\partial \dot{T}_{t_{m_2}}} + \frac{\partial \dot{q}^{(n)'}_{t_{m_2}}}{\partial \dot{T}_{t_{m_2}}}\right)\left(\dot{T}_{w_{\ell_2}} - \dot{T}^{(0)}_{w_{\ell_2}}\right)$$

$$+ \left(\frac{\partial \dot{q}^{(n)}_{w_{\ell_2}}}{\partial \dot{T}_{w_{\ell_2+1}}} + \frac{\partial \dot{q}^{(n)'}_{w_{\ell_2}}}{\partial \dot{T}_{w_{\ell_2+1}}} + \frac{\partial \dot{q}^{(n)}_{t_{m_2}}}{\partial \dot{T}_{t_{m_2-1}}} + \frac{\partial \dot{q}^{(n)'}_{t_{m_2}}}{\partial \dot{T}_{t_{m_2-1}}}\right)\left(\dot{T}_{w_{\ell_2+1}} - \dot{T}^{(0)}_{w_{\ell_2+1}}\right)$$

$$+ \sum_{j=\ell_2+2}^{\ell_3} \left(\frac{\partial \dot{q}^{(n)}_{w_{\ell_2}}}{\partial \dot{T}_{w_j}} + \frac{\partial \dot{q}^{(n)}_{t_{m_2}}}{\partial \dot{T}_{t_{m_2-(j+\ell_2)}}}\right)\left(\dot{T}_{w_j} - \dot{T}^{(0)}_{w_j}\right)$$

$$+ \sum_{j=k_1}^{k_2-2} \left(\frac{\partial \dot{q}^{(n)}_{t_{m_2}}}{\partial \dot{T}_{t_{m_2-(j-k_1)}}} + \frac{\partial \dot{q}^{(n)}_{c_{k_2}}}{\partial \dot{T}_{c_j}}\right)\left(\dot{T}_{c_j} - \dot{T}^{(0)}_{c_j}\right)$$

$$+\left(\frac{\partial \overset{*}{q}{}^{(n)}_{c_{k_2}}}{\partial \overset{*}{T}_{c_{k_2-1}}}+\frac{\partial \overset{*}{q}{}^{(n)'}_{c_{k_2}}}{\partial \overset{*}{T}_{c_{k_2-1}}}+\frac{\partial \overset{*}{q}{}^{(n)}_{t_{m_2}}}{\partial \overset{*}{T}_{t_{m_2+1}}}+\frac{\partial \overset{*}{q}{}^{(n)'}_{t_{m_2}}}{\partial \overset{*}{T}_{t_{m_2+1}}}\right)\left(\overset{*}{T}_{c_{k_2-1}}-\overset{*}{T}{}^{(0)}_{c_{k_2-1}}\right). \tag{100}$$

The solution procedure may be started by assuming initial interface temperature sensitivities, $\overset{*}{T}{}^{(0)}_{\ell}$, to be unity. Then, $\overset{*}{q}{}^{(n)(0)}_{j}$ in each zone may be obtained from the standard BEM eqn (78). The exact interface temperature sensitivities may then be determined from eqns (97)–(100). The BEM equation is used once more to determine the interface flux sensitivities along with other unknowns.

7. RESULTS FROM BEM SENSITIVITY ANALYSIS

It is assumed here that the boundary ∂B of a simply connected region may be decomposed as

$$\partial B = \partial B_{\text{no-opt}} \cup \partial B_{\text{opt}}$$

where ∂B_{opt} is the portion of the boundary being varied or optimized. Once again, steady-state turning operations are considered here. The design sensitivities of temperature and flux fields are first considered in single regions, and two example problems involving parabolic variation of shear plane geometry and gradual nose wear of a cutting tool are presented.

In metal cutting processes, the chip thickness is typically assumed to be uniform. In many situations (Trent, 1984), however, the chip thickness is not uniform. Hence, the shear angle may vary across the depth of cut, and the shear plane will also be curved. Similar situations also arise in plunge grinding. To investigate the implications of the uniform chip thickness assumption, the shear plane geometry is varied as a parabola (see Fig. 15) represented as

$$\begin{aligned} x' &= \eta \\ y' &= b(\eta-0.5)(\eta+0.5); \quad -0.5 \leqslant \eta \leqslant 0.5, \end{aligned} \tag{101}$$

where x' and y' are local tangential and normal coordinates, respectively, at the shear plane. Here, b is a parameter determining the maximum normal distance between the nominal and the perturbed parabolic shape. For example, the maximum normal distance will be $0.25b$ if the nominal shape is a straight line ($b = 0$).

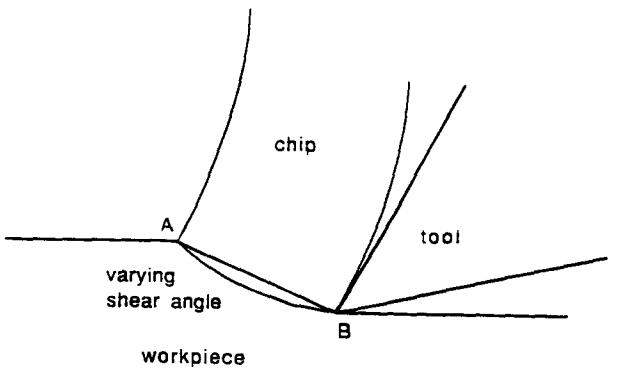

Fig. 15. Schematic diagram of shear angle variations in machining problems.

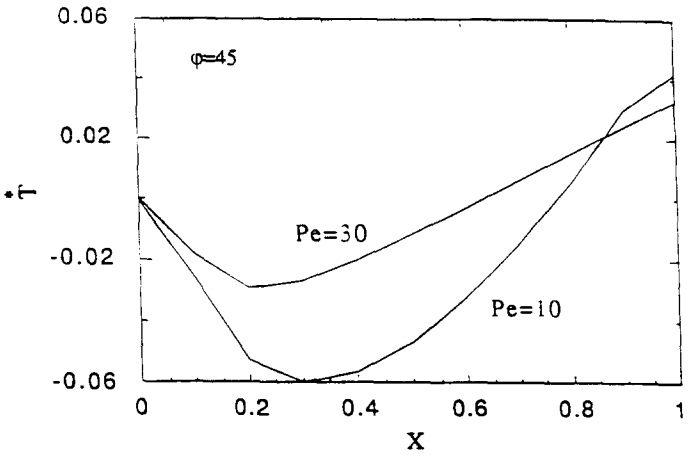

Fig. 16. Temperature sensitivities along the shear plane due to shear angle variations.

The nominal configuration is a straight line ($b = 0$). Figure 16 shows the temperature and its sensitivity along a shear plane (in the nominal configuration) for Pe = 10 and 30 at a shear angle of 45°. The abscissa is the dimensionless distance along the shear plane (see Fig. 15) measured from A ($x = 0$) to B ($x = 1$). The sensitivity of the temperature decreases with the Peclet number and, as Pe goes from 10 to 30, the maximum temperature sensitivity goes from -0.06 to -0.025. The position of the maximum also shifts toward point A (in Fig. 15).

The wear of the tool nose with machining is considered next. The nose curve is parameterized as (design parameter b represents the tool nose radius, $b = 0$ corresponds to a sharp tool)

$$x' = \eta$$

$$y' = a\left[b \exp\left(-\frac{1}{b}|\eta|\right) + |\eta|\right]; \quad -1.0 \leqslant \eta \leqslant 1.0, \tag{102}$$

where x' and y' are the local tangential and normal coordinates, respectively, at the tool nose. The parameter a is the cotangent of half of the included angle in the tool wedge, and b represents the amount of blunting of the tool nose. A perfectly sharp tool is represented by setting $b = 0$, and the blunting of the nose is repeated by increasing b. Figure 17 shows a schematic diagram of the tool wear. Figure 18 shows the temperature sensitivity along the chip-tool interface. The abscissa is the distance measured from point B in Fig. 17. In this case, the nominal configuration is of crucial importance. The temperature sensitivity increases significantly as the tool wears out. The maximum temperature sensitivity occurs

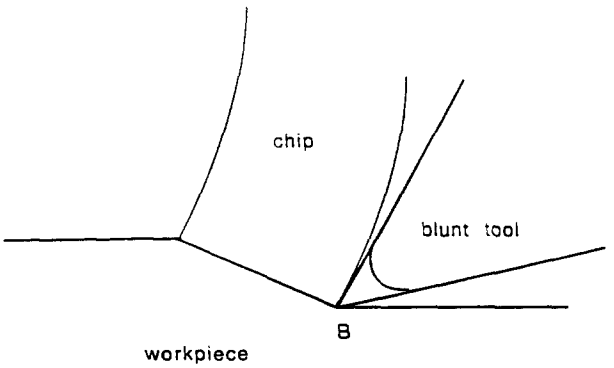

Fig. 17. Schematic diagram of gradual nose wear of a cutting tool in machining problems.

at point B and goes from 0.021 to 0.129 as b goes from 0.01 to 0.02. This also corroborates the physical observations in real-life machining operations.

As the machining process continues, the length of the flank land gradually increases. The details of the parameterization of flank wear are given in Appendix A. Figure 19 shows the temperature sensitivities along the interfaces with variations in the flank length. Figure 19(a) shows the temperature sensitivities along the workpiece-chip interface ($A-B$) and the workpiece-tool interface ($B-D$). It may be observed that the temperature sensitivity is negative for both cases of $L_{FW} = 0.4$ and 0.5 (L_{FW} = flank length/length of the shear plane). As L_{FW} increases from 0.4 to 0.5, the magnitude of the temperature sensitivity along the interfaces ABD decreases. Assuming that the flank wear rate is predominantly governed by the flank temperature, this will be expected as transition from the primary flank wear region to the secondary flank wear takes place. Figure 19(b) shows the temperature sensitivities at the chip-tool interface ($C-B$) for $L_{FW} = 0.4$ and 0.5. A similar trend is also observed at the chip-tool interface.

Figure 20 shows the flux sensitivities at the interfaces for $L_{FW} = 0.4$ and 0.5. Figure 20(a) shows the sensitivity of the flux going into the workpiece along the workpiece-chip interface. The flux sensitivity is negative in both cases, and its magnitude reduces with increase in flank length. It should be noted that flux balance must be maintained and the sensitivity of the flux going into the chip along the interface AB is positive with equal magnitude. The sensitivity of the flux going into the workpiece along the workpiece-tool interface BD is shown in Fig. 20(b). It is observed, as expected, that the flux sensitivity along BD is much higher than that at other interfaces. This is due to the fact that the flank length BD is being altered. Figure 20(c) shows the sensitivity of the flux going into the chip at the chip-tool interface CB.

Figure 21 shows the temperature sensitivities along the chip-tool interface with variations in the size of the crater. The details of the parameterization of crater wear are given in Appendix B. In our calculations, we start from a normalized (with respect to length of the shear plane) crater depth of 0.05. Since this crater size is quite small, we expect to see the transition from primary crater to secondary crater with progressive wear of the tool. It may be observed that the temperature sensitivities decrease with the increase in the size of the crater. This is expected at the transition from primary to secondary craters. The temperature sensitivity at the leading edge of the crater is negative while the sensitivities at the center and the trailing edge of the crater are positive. Accordingly, one would expect higher rates of crater wear at the center and the trailing edge. This observation also correlates well with experimental observation.

8. DISCUSSION AND CONCLUSIONS

Boundary element method (BEM) formulations for analyses and design sensitivity studies of the thermal aspects of steady-state machining processes are presented here. The

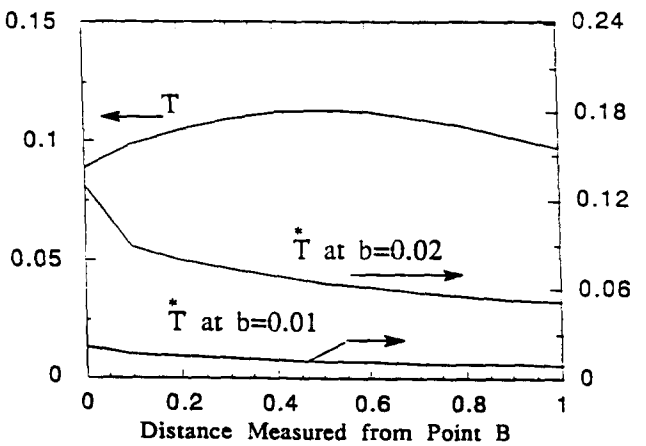

Fig. 18. Temperature sensitivities along the chip-tool interface due to gradual nose wear.

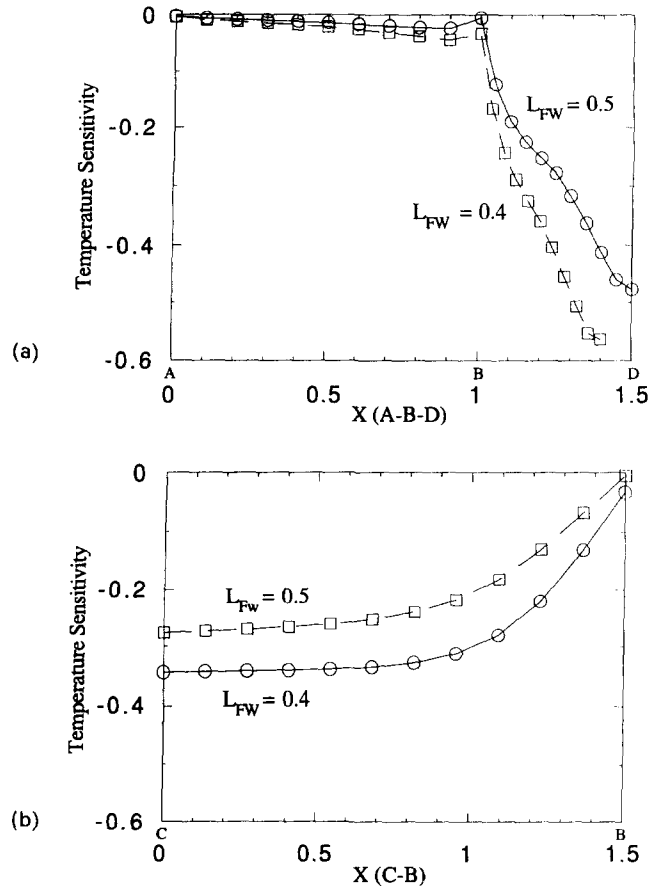

Fig. 19. Temperature sensitivities at the interfaces for two different flank lengths: (a) workpiece-chip (AB) and workpiece-tool (BD) interfaces and (b) chip-tool interface (CB).

BEM analysis algorithm is first applied to obtain the surface temperature in a semi-infinite domain with surface heating over a finite region, and the results are compared to the well-known Jaeger solutions. The BEM approach is then applied to steady-state machining operations. The analysis of the heat transfer involves applications of the BEM separately to the workpiece, the chip and the tool because of different velocities in each of these regions. A complete heat transfer model is then obtained by matching the boundary conditions across the interfaces. An exact algebraic system of equations is derived to satisfy the matching boundary conditions. This obviates the need for any iterations.

Numerical solutions of heat transfer during steady-state turning under realistic processing conditions are also presented. It is observed that the temperature along the shear plane increases with the cutting speed. The maximum temperature on the chip-tool interface approximately doubles when the Peclet number varies from 10 to 50. It is also observed that more heat is conducted into the workpiece than into the chip across the shear plane. Heat conducted into the chip across the chip-tool interface is, in turn, greater than the heat conducted into the tool. It is also found that the portion of the total heat flux going into the chip increases rapidly with the Peclet number.

A boundary element method (BEM) formulation for the determination of design sensitivities in steady-state conduction–convection problems is developed through a direct differentiation approach (DDA). This does not increase the singularity of the kernels and does retain the accuracy advantages of the BEM. The BEM formulation is based on the fundamental solution of the full adjoint equation. Accordingly, the convection term is modeled with higher precision than that obtained by upwinding in finite difference. Consequently, the BEM solution is stable regardless of the Peclet number and does not show any false diffusion. Irregular boundaries may be easily handled by the BEM. It also has the

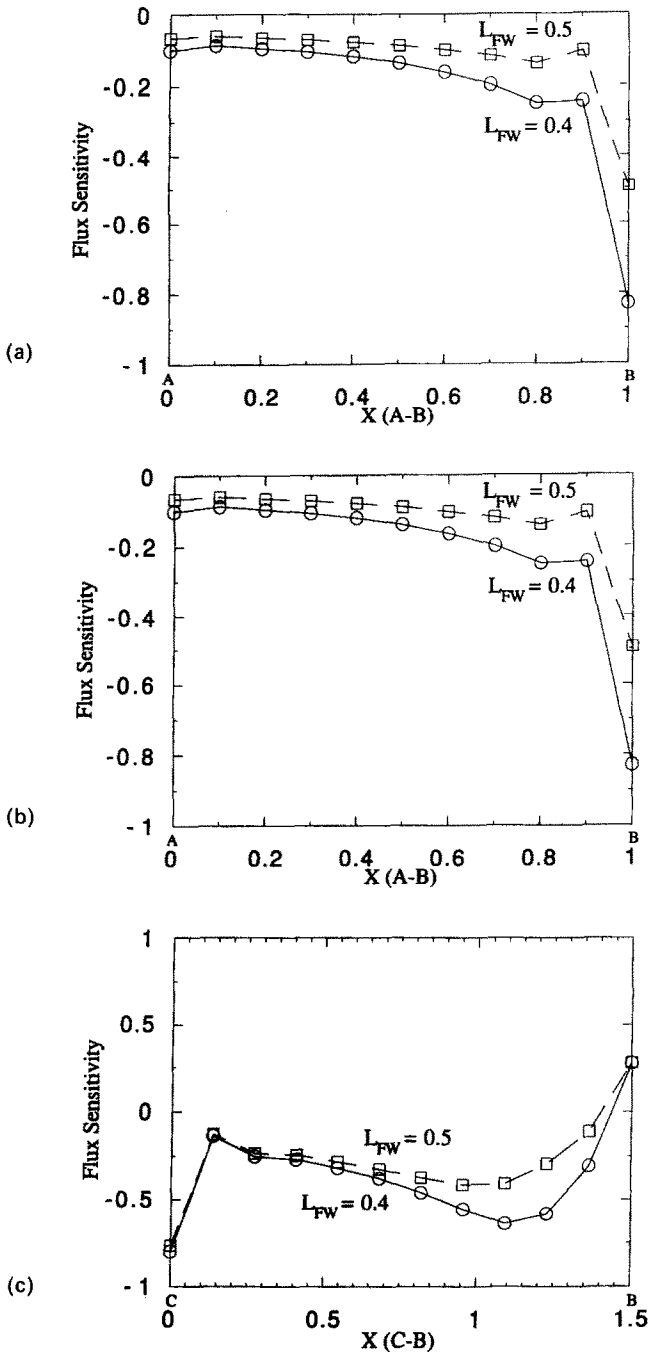

Fig. 20. Flux sensitivities at the interfaces for two different flank lengths: (a) workpiece-chip (AB) interface, (b) workpiece-tool (BD) interface, and (c) chip-tool (CB) interface.

advantage of using a smaller amount of core memory since only the boundary of the domain needs to be discretized. It is also important to note that the kernels G and $\partial G/\partial n_Q$ in eqn (77) depend on the reference configuration only and do not depend on the choice of design parameter b. All the effects for a particular choice of b are incorporated through the right-hand side vector. Accordingly, for a relatively small increase in additional cost due to evaluation of right-hand side vectors, sensitivities with respect to several design variables may be obtained simultaneously. This makes the BEM sensitivities algorithm very efficient.

The BEM is also applied to several machining problems, and the design sensitivities of temperature and flux fields are obtained with respect to several geometric and process parameters. The analysis and the sensitivity calculations involve separate applications of

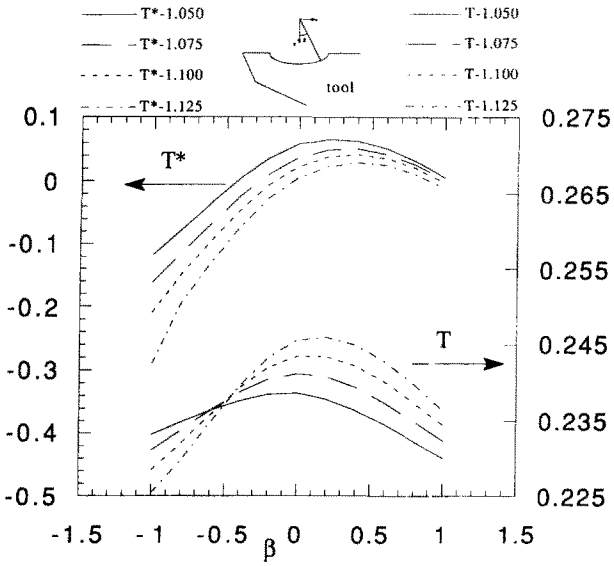

Fig. 21. Temperature and temperature sensitivities along the crater for different crater sizes.

the BEM to the workpiece, the tool and the chip regions. A complete set of results for the machining process is obtained by matching the boundary conditions across the interfaces. Exact algebraic systems of eqns (94)–(95) are derived to satisfy the matching boundary conditions. This obviates the need for any iteration.

Acknowledgements—A. Chandra's contribution to this research has been supported by Grant No. DMC-8657345 of the U.S. National Science Foundation and by Hughes Aircraft Company. C. L. Chan's contribution to this research has been supported by Grant No. CTS-8909101 of the U.S. National Science Foundation.

REFERENCES

Banerjee, P. K. and Butterfield, R. (1981). *Boundary Element Methods in Engineering Science*. McGraw-Hill, London.

Barone, M. R. and Yang, R.-J. (1988). Boundary integral equations for recovery of design sensitivities in shape optimization. *AIAA J.* **26,** 589–594.

Beskos, D. E. (ed.) (1987). *Boundary Element Methods in Mechanics*. North-Holland, Amsterdam.

Bhattacharyya, A. (1984). *Metal Cutting Theory and Practice*. Central Book Publisher, Calcutta.

Brebbia, C. A., Telles, J. C. F. and Worbel, L. C. (1984). *Boundary Element Techniques Theory and Applications in Engineering*. Springer–Verlag, Berlin.

Carslaw, H. S. and Jaeger, J. C. (1986). *Conduction of Heat in Solids*. (2nd Edn.) Clarendon Press, Oxford.

Chan, C. L. and Chandra, A. (1991a). A boundary element analysis of the thermal aspects of metal cutting. *ASME J. Engng Industry* **113,** 311–319.

Chan, C. L. and Chandra, A. (1991b). An algorithm for handling corners in the boundary element method: application to conduction–convection equations. *Appl. Math. Modelling* **15,** 244–255.

Chan, C. L. and Chandra, A. (1991c). A BEM approach to thermal aspects of machining processes and their design sensitivities. *Appl. Math. Modelling* **15,** 562–575.

Chandra, A. and Chan, C. L. (1992). A BEM formulation for design sensitivities in steady-state conduction–convection problems. *ASME J. Appl. Mech.* **59,** 182–190.

Curran, D. A. S., Lewis, B. A. and Cross, M. (1986). A boundary element method for the solutions of the transient diffusion equation in two dimensions. *Appl. Math. Modelling.* **10,** 107–113.

Dawson, P. R. and Malkin, S. (1984). Inclined moving heat source model for calculating metal cutting temperatures. *ASME J. Engng Industry* **106,** 179–186.

Fleuries, J. and Predeleanu, M. (1987). On the use of coupled fundamental solutions in BEM for thermoelastic problems. *Engng Analysis* **4,** 70–74.

Haug, E. J., Choi, K. K. and Komkov, V. (1986). *Design Sensitivity Analysis of Structural Systems*. Academic Press, New York.

Jaeger, J. C. (1942). Moving sources of heat and the temperature at sliding contacts. *Proc. R. Soc. New South Wales.* **76,** 203–224.

Lemaire, J. C. and Backofen, W. A. (1972). Adiabatic instability of the orthogonal cutting of steel. *AIME Metall. Trans.* **3,** 477–481.

Levy, E. K., Tsai, C. L. and Groover, M. P. (1976). Analytical investigation of the effect of tool wear on the temperature variations in a metal cutting tool. *ASME J. Engng Industry* **98,** 251–257.

Loewen, E. G. and Shaw, M. C. (1954). On the analysis of cutting tool temperatures. *Trans. ASME* **76,** 217–221.

Mukherjee, S. (1982). *Boundary Element Methods in creep and fracture*. Elsevier Applied Science, Barking.

Mukherjee, S. and Chandra, A. (1989). A boundary element formulation for design sensitivities in materially nonlinear problems. *Acta Mechanica.* **78,** 243–253.
Mukherjee, S. and Chandra, A. (1991). A boundary element formulation for design sensitivities in problems involving both geometric and material nonlinearities. *Int. J. Math. Comput. Modelling* **15,** 245–255.
Muraka, P. D., Barrow, G. and Hinduja, S. (1979). Influence of the process variables on the temperature distribution in orthogonal machining using the finite element method. *Int. J. Mech. Sci.* **21,** 445–456.
O'Neill, K. (1983). Boundary integral equation solution of moving boundary phase change problems. *Int. J. Numer. Meth. Engng* **19,** 1825–1850.
Press, W. H., Flannery, B. P., Teukolsky, S. A. and Vetterling, W. T. (1986). *Numerical Recipes.* Cambridge University Press, New York.
Ramalingam. S., Basu, K. and Malkin, S. (1977). Deformation index of MnS inclusions in resulferized and leaded steels. *Mater. Sci. Engng* **29,** 117–121.
Rice, J. S. and Mukherjee, S. (1990). Design sensitivity coefficients for axisymmetric elasticity problems by boundary element methods. *Engng Anal. Boundary Elements* **7,** 13–20.
Saigal, S., Borgaard, J. T. and Kane, J. H. (1989). Boundary element implicit differentiation equations for design sensitivities in axisymmetric structures. *Int. J. Solids Structures* **25,** 527–538.
Shaw, M. C. (1984). *Metal Cutting Principles.* Clarendon Press, Oxford.
Stevenson, M. G., Wright, P. K. and Chow, J. G. (1983). Further developments in applying the finite element method to the calculation of temperature distributions in machining and comparisons with experiment. *ASME J. Engng Industry* **105,** 149–154.
Tanaka, Y., Honma, T. and Kaji, I. (1986). On mixed boundary element solutions of convection–diffusion problems in three-dimensions. *Appl. Math. Modelling* **10,** 170–175.
Tay, A. E., Stevenson, M. G. and DeVahl Davis, G. (1974). Using the Finite Element Method to determine temperature distributions in orthogonal machining. *Proc. Institute of Mechanical Engineers* **188**(55), 627–638.
Trent, E. M. (1984). *Metal Cutting.* Butterworths, London.
Tsay, J.-J. and Arora, J. S. (1988). Design sensitivity and analysis of nonlinear structures with history dependent effects. Technical report No. ODL-88.4, University of Iowa, Iowa City.
Von Turkovich, B. F. (1972). On a class of thermo-mechanical processes during rapid plastic deformation (with special reference to metal cutting). *Annals of the CIRP* **21,** 15–16.
Zabaras, N. and Mukherjee, S. (1987). An analysis of solidification problems by the boundary element method. *Int. J. Numer. Meth. Engng* **24,** 1879–1900.
Zabaras, N., Mukherjee, S. and Richmond, O. (1988). An analysis of inverse heat transfer problems with phase changes using an integral method. *J. Heat Transfer* **110,** 554–561.

APPENDIX A. PARAMETERIZATION OF FLANK WEAR

As the machining process continues, the length of the flank land gradually increases. As the flank land develops, the tool is fed in the direction perpendicular to the cutting velocity. In the present work, the flank wear is modeled by seven different regions, as shown schematically in Fig. A1. Here, b is the design variable representing the amount of wear perpendicular to the flank land and x' and y' are, respectively, the local tangential and normal coordinates. In our convection, the origin for a region is set at the starting point for that region (e.g. the origin for the region a–b is at point "a").

Region I (a–b):

$$x' = \left(\Delta s_{ab} - \frac{b}{\sin\theta}\right)\frac{\eta}{\Delta s_{ab}} \quad 0 \leqslant \eta \leqslant \Delta s_{ab},$$
$$y' = 0 \tag{A.1}$$

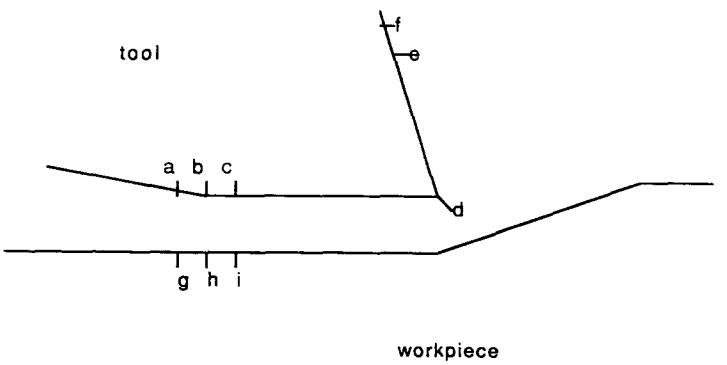

Fig. A1. Schematic diagram of flank wear in machining.

Region 2 (b–c):

$$x' = -b\cot\left\{(\theta-\alpha)\frac{\Delta s_{bc}-\eta}{\Delta s_{bc}}+\alpha\right\} \quad 0 \leqslant \eta \leqslant \Delta s_{bc},$$
$$y' = b \tag{A.2}$$

Region 3 (c–d):

$$x' = \eta - b\tan\alpha \quad 0 \leqslant \eta \leqslant \Delta s_{cd},$$
$$y' = b \tag{A.3}$$

Region 4 (d–e):

$$x' = \eta - \frac{b}{\cos\alpha} \quad 0 \leqslant \eta \leqslant \Delta s_{de},$$
$$y' = 0 \tag{A.4}$$

Region 5 (e–f):

$$x' = \frac{\Delta s_{ef} - \dfrac{b}{\cos\alpha}}{\Delta s_{ef}}(\Delta s_{ef}+\eta) \quad 0 \leqslant \eta \leqslant \Delta s_{ef},$$
$$y' = 0 \tag{A.5}$$

Region 6 (g–h):

$$x' = \frac{\Delta s_{gh} - b[\tan(\pi/2-\theta)-\tan\alpha]}{\Delta s_{gh}}\eta \quad 0 \leqslant \eta \leqslant \Delta s_{gh},$$
$$y' = 0 \tag{A.6}$$

Region 7 (h–i):

$$x' = \frac{\Delta s_{hi} - b[\tan(\pi/s-\theta)-\tan\alpha]}{\Delta s_{hi}}(\Delta s_{hi}-\eta) \quad 0 \leqslant \eta \leqslant \Delta s_{hi},$$
$$y' = 0. \tag{A.7}$$

APPENDIX B. PARAMETERIZATION OF CRATER WEAR

As the machining process continues, the size of the crater at the tool-chip interface gradually increases. In the present work, the crater is modeled as an arc of a circle (shown schematically in Fig. B1), and crater wear is modeled by six regions. It is assumed that the crater is small so that the chip is basically undeformed. Here, R is the design variable representing the radius of the arc, h is the perpendicular distance from the center of the crater to the original rake face of the tool, and x' and y' are, respectively, the local tangential and normal coordinates. In our convection, the origin for a region is set at the starting point for that region (e.g. the origin for the region a–b is at point "a"). The only exception is region 2, where the origin is set at the center of the crater.

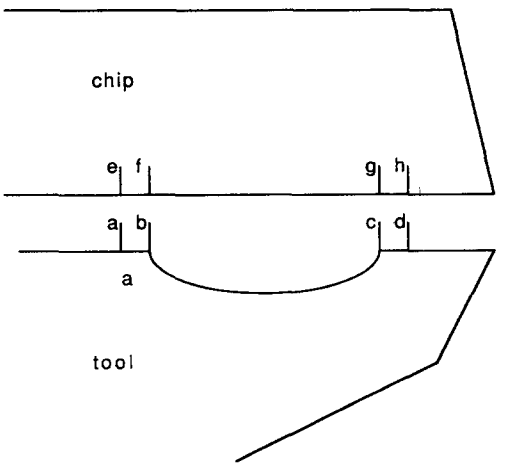

Fig. B1. Schematic diagram of crater wear in machining.

Region 1 (a–b):

$$x' = -\frac{\eta}{\Delta s_{ab}} R \sin\left[\cos^{-1}\left(\frac{h}{R}\right)\right] \quad 0 \leqslant \eta \leqslant \Delta s_{ab},$$
$$y' = 0 \tag{B.1}$$

Region 2 (b–c):

$$x' = R \sin\left[\eta \cos^{-1}\left(\frac{h}{R}\right)\right]$$
$$y' = R \cos\left[\eta \cos^{-1}\left(\frac{h}{R}\right)\right],$$

where

$$\eta = \frac{\beta}{\cos^{-1}\left(\frac{h}{R_0}\right)} \quad \text{and} \quad \beta = \tan^{-1}\left(\frac{x'_0}{y'_0}\right). \tag{B.2}$$

Here, the subscripted zero denotes a reference crater configuration.

Region 3 (c–d):

$$x' = \left(1 - \frac{\eta}{\Delta s_{cd}}\right) R \sin\left[\cos^{-1}\left(\frac{h}{R}\right)\right] \quad 0 \leqslant \eta \leqslant \Delta s_{cd},$$
$$y' = 0 \tag{B.3}$$

Region 4 (e–f):

$$x' = -\frac{\eta}{\Delta s_{ef}} R \sin\left[\cos^{-1}\left(\frac{h}{R}\right)\right] \quad 0 \leqslant \eta \leqslant \Delta s_{ef},$$
$$y' = 0 \tag{B.4}$$

Region 5 (f–g):

$$x' = 2\frac{\eta}{\Delta s_{fg}} R \cos^{-1}\left(\frac{h}{R}\right) - R \sin\left[\cos^{-1}\left(\frac{h}{R}\right)\right] \quad 0 \leqslant \eta \leqslant \Delta s_{fg},$$
$$y' = 0 \tag{B.5}$$

Region 6 (g–h):

$$x' = \left(1 - \frac{\eta}{\Delta s_{gh}}\right)\left\{2R \cos^{-1}\left(\frac{h}{R}\right) - R \sin\left[\cos^{-1}\left(\frac{h}{R}\right)\right]\right\} \quad 0 \leqslant \eta \leqslant \Delta s_{gh}.$$
$$y' = 0 \tag{B.6}$$